Multiscale synchrotron microtomography imaging of kerogen lenses in organic-rich shales from the Norwegian Continental Shelf

James Ronald Johnson [a,*], Maya Kobchenko [a], Nazmul Haque Mondol [a,c], François Renard [a,b]

[a] Department of Geosciences, The Njord Centre, University of Oslo, P.O. Box 1047, Blindern, NO-0316 Oslo, Norway
[b] University Grenoble Alpes, University Savoie Mont Blanc, CNRS, IRD, ISTerre, 38000 Grenoble, France
[c] Norwegian Geotechnical Institute (NGI), P.O. Box 3930, Ullevaal Stadion, NO-0806 Oslo, Norway

ARTICLE INFO

ABSTRACT

Kerogen lens shape and size distribution control how organic-rich shales may behave as either source or seal rocks. Prior to thermal conversion, kerogen is a brittle, load-bearing constituent of the shale matrix. During thermal maturation, kerogen lenses become more ductile, and hydrocarbon expulsion may lead to the creation of microfractures, a process controlled not only by temperature and pressure but also by the size and shape of kerogen lenses and their total content in the rock. Here, we use high-resolution multiscale synchrotron micro-tomography imaging of centimeter-scale shale rock samples collected in two boreholes at different depths in the North Sea and the Barents Sea, respectively. From these three-dimensional microtomography data, we quantify the various shapes of kerogen lenses and discuss how each step of a kerogen lens's life-cycle (i.e. original bio-logical structure, deposition, degradation, and diagenesis) impacted its shape before catagenesis. We quantify the relationship between kerogen volume and the number of kerogen lenses in a given rock volume. The relationship between total organic carbon (TOC) content and the average kerogen lens volume is also measured. For a given rock volume, results show that organic content increases with the number of kerogen lenses up to a point (~8–12 wt% TOC) above which TOC continues to increase, but the number of kerogen lenses decreases. These results combined with kerogen lens orientation may control microfracturing during kerogen maturation.

1. Introduction

Organic-rich shales are studied for their importance for many geo-engineering purposes. Understanding organic-rich shales as the source or seal rocks are critical to hydrocarbon exploration in both conventional and unconventional plays (Prasad et al., 2011; Bourg, 2015; Johnson, 2017; Hansen et al., 2020; Johnson et al., 2022). The presence of microfractures in mature or partially mature shales controls their quality as a seal, which is important for subsurface CO_2 storage as well as for the disposal of nuclear wastes (Bourg, 2015). Microfracturing occurring during kerogen maturation in organic-rich shales has been proposed to be driven predominantly by volume expansion of kerogen lenses due to hydrocarbon production (Hunt, 1996; Vernik, 1994; Lash and Engelder, 2005; Fan et al., 2010; Jin et al., 2010; Kobchenko et al., 2011; Panahi et al., 2019; Voltolini and Franklin, 2020). The coupling between kerogen maturation and microfracture growth has a critical impact on the geomechanical properties of shales and whether shales behave as a source or seal rocks (Vernik, 1994; Anders et al., 2014;

Chauve et al., 2020; Voltolini and Franklin, 2020; Liu et al., 2021). Understanding shale as a seal for CO_2/water systems is inherently more complex due to reactivity of the mineralogy (Busch et al., 2016; Kalani, 2018; Skurtveit et al., 2018), miscibility of the fluids (Kalani, 2018; Skurtveit et al., 2018), and capillary sealing behavior (Kalani, 2018). Finally, understanding the presence and fabric of shales is critical to geotechnical investigations (Nichols et al., 1986; Nichols, 1992; Sabtan, 2005, Okewale and Grobler, 2020).

The distribution of organic matter present in shale and the degree of maturation that shale has undergone control the mechanical properties of this rock. When the shale is immature, the organic matter acts as a brittle, load-bearing constituent within the matrix (Prasad et al., 2009; Prasad et al., 2011; Brochard et al., 2013; Mondol, 2018; Johnson et al., 2022). The chemical composition of kerogen lenses, which depends on kerogen type, influences the dynamic modulus (Alstadt et al., 2016; Bousige et al., 2016; Shitrit et al., 2016). As maturation progresses, kerogen lenses become increasingly ductile, while both their surface area and volume increase (Kelemen et al., 2006; Craddock et al., 2018;

Craddock et al., 2019) until hydrocarbon expulsion occurs, at which point the mineral grains become load-bearing (Prasad et al., 2009; Prasad et al., 2011; Johnson et al., 2022). During this process, it has been suggested that porosity internal to kerogen will be created, and that this will have an impact on the material properties of the shale (Alfred and Vernik, 2013; Pepper, 2017). However, at this point, a network of fractures may have also formed due to the conversion process (Fan et al., 2010; Jin et al., 2010; Fan et al., 2012; Chauve et al., 2020; Voltolini and Franklin, 2020). The lithostatic load can control the phase equilibrium between kerogen and the hydrocarbons expelled (Pepper and Corvi, 1995; Carcione and Avseth, 2015; Burnham, 2017; Pepper, 2017). Lithostatic load also influences the amount of porosity generated due to the microfracturing process (Pepper and Corvi, 1995; Carcione and Avseth, 2015; Burnham, 2017; Pepper, 2017). When considering the seal capacity of an immature shale, the volume percentage of organic material controls the geomechanical properties (e.g., Young's modulus, shear modulus, bulk modulus, Poisson's ratio). In contrast, when shale has undergone thermal maturation and microfractures were produced, the degree of microfracture healing and sealing controls the geomechanical properties (Voltolini and Franklin, 2020). This effect is related to the impact that porosity, both internal to kerogen lenses and created by microfractures, has on the material properties of shale (Eliyahu et al., 2015).

While organic-rich shale may behave as a seal rock, both before and after the hydrocarbon expulsion process, during hydrocarbon expulsion, shale becomes increasingly brittle with the growth of microfractures that nucleate at kerogen lenses. This process has been proposed and documented on a variety of scales (Pelet and Tissot, 1971; Vernik, 1994; Fan et al., 2010; Jin et al., 2010; Teixeira et al., 2017; Johnson et al., 2019; Chauve et al., 2020; Voltolini and Franklin, 2020). Numerical modeling studies have shown that the size of the kerogen lenses controls the rate of microfracture growth and ultimately, microfracture lengths (Fan et al., 2010; Fan et al., 2012). The size and spatial distribution of the kerogen lenses dictate the connectivity of the microfracture network that leads to hydrocarbon expulsion (Jin et al., 2010; Chauve et al., 2020; Liu et al., 2021). Finally, the shape of the kerogen lens can control microfracture growth direction during hydrocarbon expulsion (Li and Zhang, 2021; Chauve et al., 2020) and the geomechanical properties of the rock afterward (Dietrich, 2015).

The fabric of shales is influenced by both the organic and inorganic components (Eliyahu et al., 2015) as they are altered during depositional and diagenetic processes, and has been shown to influence mechanical properties, degree of anisotropy, and rate of maturation (Dewhurst and Siggins, 2006; Shitrit et al., 2016; Rahman et al., 2017). In order to characterize the microstructure of organic-rich shales (i.e.,> 2% organic content), it is important to separate out the organic and inorganic components. The primary focus of our study seeks to characterize the three-dimensional properties of the organic content (i.e., kerogen lenses) within shales that come from two main source rocks in the Norwegian Continental Shelf, the Draupne Formation in the North Sea and the Hekkingen Formation in the Barents Sea. We have obtained the shales samples from two boreholes drilled in these formations, and samples were collected at depths in the range 1360–2583 m. Dominantly Type II, Type II-S, and Type III kerogens were encountered. No internal kerogen porosity was identified, which falls in line with the maturation state of the samples collected. Using multiscale microscopy and synchrotron X-ray microtomography imaging, we determine the shape, size, and distribution of kerogen lenses in the shales and discuss how these parameters may influence the geomechanical properties of the rock. Note, the mechanical properties will determine yield stress and influence creep behavior. We explore how the kerogen lenses may control microfracture growth and coalescence as a part of the kerogen maturation process. The inorganic content of these two shales (i.e., mineralogy) is also quantified in order to provide a framework for understanding the shales as potential sources or seals. This includes an understanding of the shale fabric, which depends on the deposition

environment (i.e., lacustrine, transitional, marine), and degree of diagenesis (Dewhurst and Siggins, 2006; Jiang et al., 2017; Rahman et al., 2017). We propose standard kerogen lens shapes tied to aspect ratios that are better representative of reality than what is currently being used for numerical modeling. Then, we develop a relationship between kerogen lens volume and the number of lenses of a given size. Furthermore, when a shale contains more than ~8–12 wt% total organic carbon content, the spatial density of kerogen lenses decreases, which is explained by the presence of larger kerogen lenses in the rock. We discuss how these results combined with kerogen lens orientation control the growth of microfractures during the maturation of organic-rich shales.

2. Geological setting and organic-rich shale samples

2.1. Upper Jurassic source rocks in the Norwegian Continental Shelf and Barents Sea

In the Norwegian Continental Shelf, both the Upper Jurassic Draupne and Hekkingen Formations contain organic-rich shales. They are major source rocks of their respective petroleum systems, typical of the Kimmeridge clay formations deposited from the Oxfordian to Ryazanian age (NPD, 2021). These shales are both described in the literature as being dark grey to black, usually non-calcareous, occasionally fissile claystones (Hansen et al., 2020; Rahman et al., 2020; NPD, 2021; Johnson et al., 2022). The Draupne Formation is a source rock distributed in the East Shetland Basin, the Viking Graben, and over the Horda Platform. While the Draupne and Hekkingen formations are considered equivalent shales, both with major source rock potential, key differences exist in their respective geological histories, resulting in significant distinctions between them (Hansen et al., 2020; Johnson et al., 2021; Johnson et al., 2022). Both formations also act as seals, with the Draupne Formation being critical to future CCUS projects in the North Sea (Johnson et al., 2021; Rahman et al., 2021; Johnson et al., 2022).

The deposition of the Draupne Formation was influenced by two major rifting events that occurred in the Norwegian North Sea (Ziegler, 1992; Faleide et al., 2008). The first event occurred in the Triassic, followed by post-rifting quiescence. This event was followed by a second larger rifting event that occurred in the Late Jurassic – Early Cretaceous forming significant structural relief within the region (Whipp et al., 2014). Coupled with eustatic sea-level rise, the subsequent anoxic, restricted environment was ideal for deep marine anaerobic conditions leading to the deposition of a source rock shale (Hansen et al., 2020; NPD, 2021). Thickness ranges from ~0 to 550 m, with the total depth range measured from wells in the Norwegian North Sea being from ~600 to 6500 m (Hansen et al., 2020; Johnson et al., 2021; NPD, 2021; Johnson et al., 2022). A typical range of total organic carbon (TOC) content for the Draupne Formation is 2–15 wt% with a mean value around 8.5 wt% (Hansen et al., 2020; Johnson et al., 2021). Kerogen type is predominantly Type II and Type II-S, with some Type III (Zadeh et al., 2017; Johnson et al., 2021; present study). Within the area studied, the mineralogy of the Draupne shales is relatively homogeneous with 40–70 wt% clay, 20–60 wt% quartz, and feldspar, and 0–20 wt% carbonate and pyrite (Hansen et al., 2020; Rahman et al., 2020; Johnson et al., 2021). Mineralogical compositions by weight percentage show a much larger proportion of soft minerals than hard minerals, with an average ratio of 2:1 (Rahman et al., 2020; Johnson et al., 2021; present study).

Like the Draupne Formation, the Hekkingen Formation underwent two rifting events, combined with eustatic sea level rise, resulting in a restricted marine ideal for the deposition of organic-rich shales environment (Dore et al., 1985; Hansen et al., 2020; NPD, 2021). Unlike the Draupne Formation in the North Sea, the Barents Sea experienced multiple uplift, and erosion episodes with estimates uplift around 1–1.2 km in the study area resulting in a diminished thickness for the Hekkingen Formation in the range ~ 0–100 m (NPD, 2021; Henriksen et al.,

2011; Baig et al., 2016). Furthermore, the erosion events in the Barents Sea coincide with significant exhumation that varies from 0.4 to 3.0 km, with an approximate 1.3 km of exhumation at well 7125/1–1 (Fig. 1b, Zadeh et al., 2017, Baig et al., 2019, Ohm et al., 2008; Henriksen et al., 2011; Baig et al., 2016). The large variation in the exhumation and subsequent erosion is correlated to localized salt remobilization (Muller et al., 2019). As a result, the present-day depth ranges for the Hekkingen Formation measured from wells in the Barents Sea is both narrower and shallower, from ~500 to 4300 m, than for the Draupne Formation (NPD, 2021). Despite the Hekkingen Formation being thinner, it is a prolific source rock with typical TOC content of 5–20 wt%, and a mean value of 12.2 wt% (Hansen et al., 2020). Kerogen type is predominantly Type II and Type II-S, with some Type III present (Abay, 2017; Johnson et al., 2019; Johnson et al., 2021). Mineralogical analyses within the area studied show that the Hekkingen Formation shales are composed of 60–70 wt% clay, 30–40 wt% quartz and feldspar, and 10–20 wt% carbonate and pyrite (Hansen et al., 2020; Johnson et al., 2021). Mineralogical compositions by weight percentage show a much higher proportion of soft minerals than hard minerals in the Hekkingen Formation, with the average ratio being 3:1 (Hansen et al., 2020; Johnson et al., 2021; present study).

Some broad similarities exist between the Draupne and Hekkingen Formations, including a shared depositional story. However, some clear and marked differences also exist. Notably, the Hekkingen Formation typically contains a higher clay percentage, while the Draupne Formation contains relatively more quartz and feldspar. Carbonate contents in both formations are roughly equal and considered low. Additionally, the Hekkingen Formation has a tendency to be a richer source rock with both a higher average and a greater range of TOC values than the Draupne Formation. The combination of these data indicate that the Hekkingen Formation was formed in a more restricted, more anaerobic environment than the Draupne Formation (Johnson et al., 2021). Subsequent diagenetic histories for the two formations are much different. While the Hekkingen Formation experienced significant erosion and exhumation in the Barents Sea as a result of salt remobilization, the Draupne Formation experienced comparatively little erosion in the Norwegian North Sea. Increased clay content and increased kerogen content have countermanding impacts on the geomechanical nature of the shale (Mondol et al., 2007; Brochard et al., 2013; Mondol, 2018; Johnson et al., 2021). Previous studies suggest that the samples for this study reached roughly equivalent depths (Baig et al., 2016; Zadeh et al., 2017; Baig et al., 2019); however, this depth does not necessarily correlate to equivalent maturation. Contrary to this, Johnson et al. (2021) showed that both geochemical and rock physics data support that
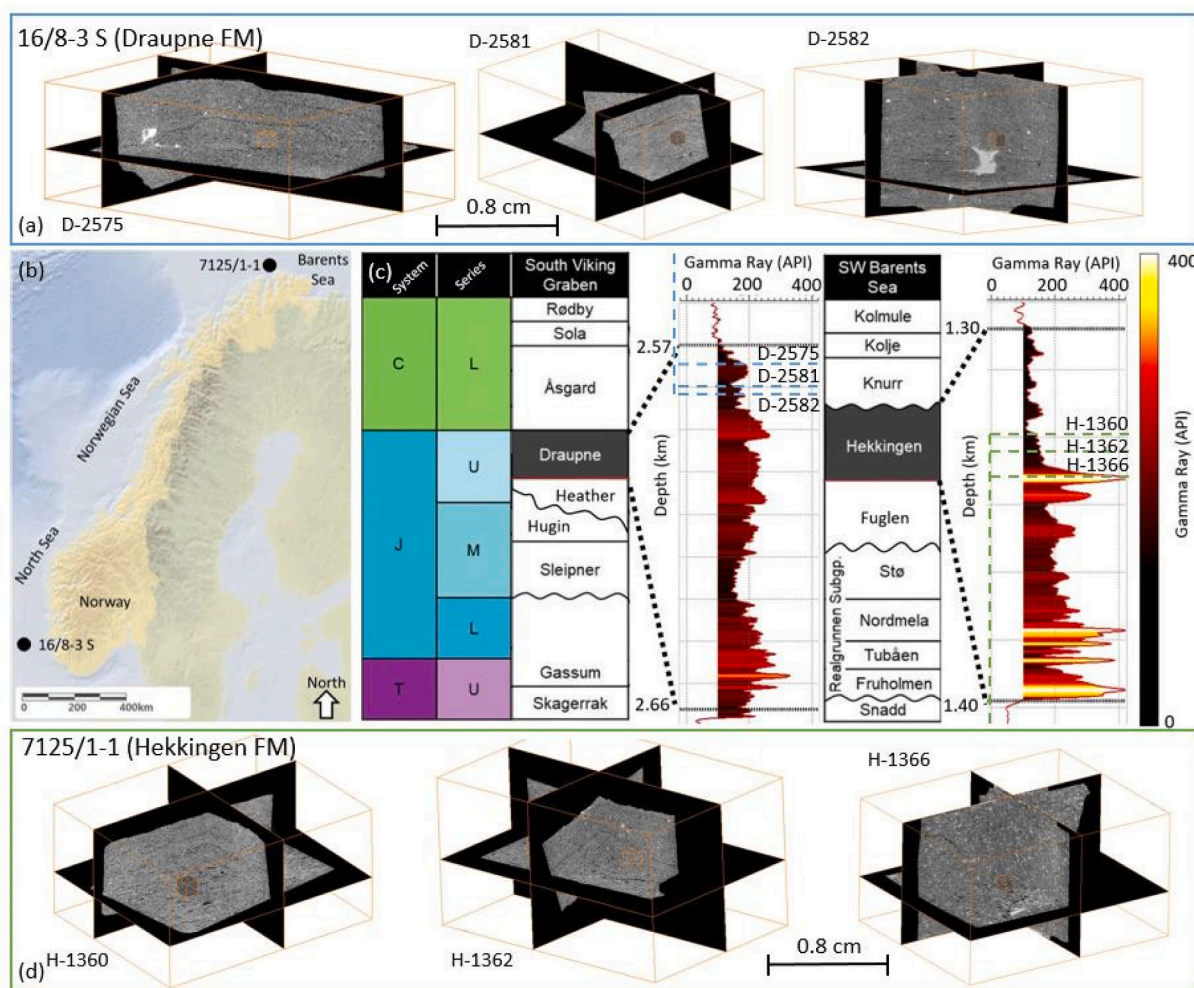

Fig. 1. (a) Synchrotron -ray microtomography images from three samples from the Draupne Formation with data collected at two spatial resolutions. The large cubes indicate the edges for the low-resolution scan (voxel size 6.63 μm), and the small cubes indicate the edges of the high-resolution scan (voxel size 0.7 μm). (b) Map showing the location of the two wells the samples were taken from. The Draupne Formation (well 16/8–3-5) samples are from the North Sea, and the Hekkingen Formation samples (well 7125/1–1) are from the Barents Sea. (c) The geological timeline given with Gamma Ray well logs for the two wells show that the Draupne and Hekkingen Formations are both organic-rich shales. The six samples, three from each formation, have depth labels and sample numbers indicated on the Gamma Ray log. (d) Synchrotron X-ray microtomography images from three samples from the Hekkingen Formation with the data collected at two resolutions.

the Draupne shale samples collected in well 16/8–3 S are immature and ductile in nature, while the Hekkingen shale samples collected in well 7125/1–1 are in the early oil generation window and are comparatively in the transition towards becoming more brittle as a result of kerogen maturation. Some limited oil and gas expulsion may have begun to occur for the Hekkingen shale samples, while this should not be the case for the Draupne shale samples.

2.2. Organic-rich shale samples

The six shale samples were collected at depth from borehole cores with three samples in the well 16/8–3 S drilled in the Draupne Formation and three samples in the well 7125/1–1 drilled in the Hekkingen Formation (Table 1, Fig. 1). Well logs were used to verify the sample's exact location and compare logging data with microstructural observations and geochemical measurements using the Rock-Eval technique. The depth range of the Draupne Formation in well 16/8–3 S is 2570–2660 m, with shale samples collected in the range 2575–2583 m and the depth range of the Hekkingen Formation in well 7125/1–1 is 1300–1400 m, with shale samples collected in the range 1360–1367 m (Fig. 1b).

3. Methods

3.1. Multiscale synchrotron microtomography imaging

For the six shale samples, a one centimeter core was drilled and imaged in three dimensions using synchrotron X-ray microtomography. Images were acquired on the beamline ID19 at the European Synchrotron Radiation Facility in Grenoble, France. X-ray adsorption data were collected at two different spatial resolutions. Each centimeter-scale core sample was scanned entirely with a spatial sampling of 6.63 μm/voxel and an energy of 110 keV. Then, a zoom located in the middle of the sample was acquired using a local microtomography technique with a spatial sampling of 0.7 μm/voxel and an energy of 115 keV (Fig. 1). X-ray adsorption data were reconstructed using a phase retrieval reconstruction algorithm (Mittone et al., 2017). The spatial resolution of the images was not measured, but a previous study indicated that it is between two and three times the voxel size (Mittone et al., 2017). The 16-bit images were saved in TIFF format and converted to 8-bit format for further processing. We verified that the conversion from 16-bit to 8-bit did not change the results shown below on all samples.

To process the data, we developed an image analysis workflow that includes a correction for the background variation, denoising, thresholding, and segmentation (Fig. 2). We used the image processing software AvizoFire (Avizo Reference Manual, 2021). The beam hardening artifact is corrected by identifying and removing the background from the original grayscale 3D image. To preserve the kerogen lens shape and denoise the image, a non-local means filter is used (Buades et al., 2011). This filter combines Gaussian smoothing and edge-preserving techniques to account for the kerogen boundaries. In order to separate the kerogen lenses, a unique threshold was determined for each shale

sample. To enhance the results of the thresholding, a watershed algorithm is utilized to fill in local minima on the greyscale image that is a part of the kerogen lens without filling in the same pixels elsewhere in the 3D image. After thresholding, the image segmentation procedure allows separating the various kerogen lenses and microfractures from one another and labels them by different numbers and colors (Fig. 3). Few open microfractures have the same adsorption range as the kerogen lenses, and they were removed manually from the segmented image (Fig. 3).

After the images were segmented, we performed a series of quantitative analyses on the kerogen lenses such as volume fraction, size distribution, shape, smoothness, and dominant orientation. All calculations were carried out for the images of both 6.63 μm and 0.7 μm voxel sizes. The volume fraction of the kerogen lenses (v. %) was calculated by summing the volume of all lenses and dividing by the total volume of the 3D sample. To quantify the spatial distribution of the kerogen lenses inside the shale matrix, we calculated the position of the center of mass for each kerogen lense along each axis of the 3D image. These measurements were performed only on the images with 0.7 μm voxel size where the high-resolution allows separating each kerogen lens unambiguously.

To analyze kerogen lens shape and orientation in three dimensions, we calculated the 3D inertia matrix of each kerogen lense.

$$\mathbf{M_{3D}} = \begin{vmatrix} M_{xx} & M_{xy} & M_{xz} \\ M_{xy} & M_{yy} & M_{yz} \\ M_{xz} & M_{yz} & M_{zz} \end{vmatrix} \tag{1}$$

and then we calculated the three eigenvalues of the inertia matrix, $\lambda_1 > \lambda_2 > \lambda_3$ (Fig. 4). If the shape of a kerogen lens was a perfect ellipsoid, these three eigenvalues would correspond to the lengths of the three axes of the ellipsoid. For each kerogen lens, we also calculated three other parameters, the anisotropy, A_{3D}, the flatness, F_{3D}, and the elongation, E_{3D}, defined as:

$$A_{3D} = 1 - \frac{\lambda_3}{\lambda_1}; F_{3D} = \frac{\lambda_3}{\lambda_2}; E_{3D} = \frac{\lambda_2}{\lambda_1} \tag{2}$$

These three shape parameters have values in the range 0–1.

The dominant direction of a kerogen lens is defined by the orientation of the largest eigenvector of the inertia matrix. This direction is measured with two angles, θ and φ, which describe the orientation of the largest eigenvector relative to the x-axis and the z-axis of the 3D image, respectively (Fig. 4). Because the core samples were cored perpendicular to bedding, the z-direction is perpendicular to bedding and the XY plan is the bedding plane.

We also use the shape parameters α and β that describe the distribution of data in a range [0–1] (Rose and Smith, 2002). The probability density function of a given variable, x, is fitted with a function that contains two exponents, α and β:

$$f(x; \alpha, \beta) = \frac{x^{\alpha-1}(1-x)^{\beta-1}}{B(\alpha, \beta)} \tag{3}$$

Table 1
List of shale samples (D = Draupne, H = Hekkingen) used in the present study, with depth, temperature (from Bottom Hole Temperature, BHT), and mineralogical composition.

Sample	Depths (m)	Temperature (°C)	Mineralogy
D-2575	2575.30	86.2	Mixed clays (illite, kaolinite), quartz, pyrite, micas (muscovite), calcite, dolomite, siderite, apatite
D-2581	2581.65	86.4	Mixed clays (illite, kaolinite, smectite), quartz, pyrite, micas (muscovite), albite, calcite, dolomite, siderite, chlorite
D-2582	2582.15	86.4	Mixed clays (illite, kaolinite), quartz, pyrite, albite, calcite, dolomite, siderite, chlorite, rutile, sphalerite
H-1360	1360.85	48.2*	Mixed clays (illite, kaolinite), quartz, pyrite, micas (muscovite, biotite), potassium feldspar, calcite, dolomite
H-1362	1362.55	48.3*	Mixed clays (illite, kaolinite), quartz, pyrite, micas (muscovite), potassium feldspar, calcite, dolomite, apatite, rutile
H-1366	1366.40	48.4*	Mixed clays (illite, kaolinite), quartz, pyrite, micas (muscovite, biotite), potassium feldspar, calcite, sphalerite

* While the Draupne Formation shale (North Sea) is now situated at greater depth than the Hekkingen Formation shale (Barents Sea), the Barents Sea samples have been uplifted ~1300 m (Zadeh et al., 2017; Baig et al., 2019). Therefore, the Hekkingen Formation shale samples have undergone temperatures greater than 80 °C in the past (Zadeh et al., 2017).
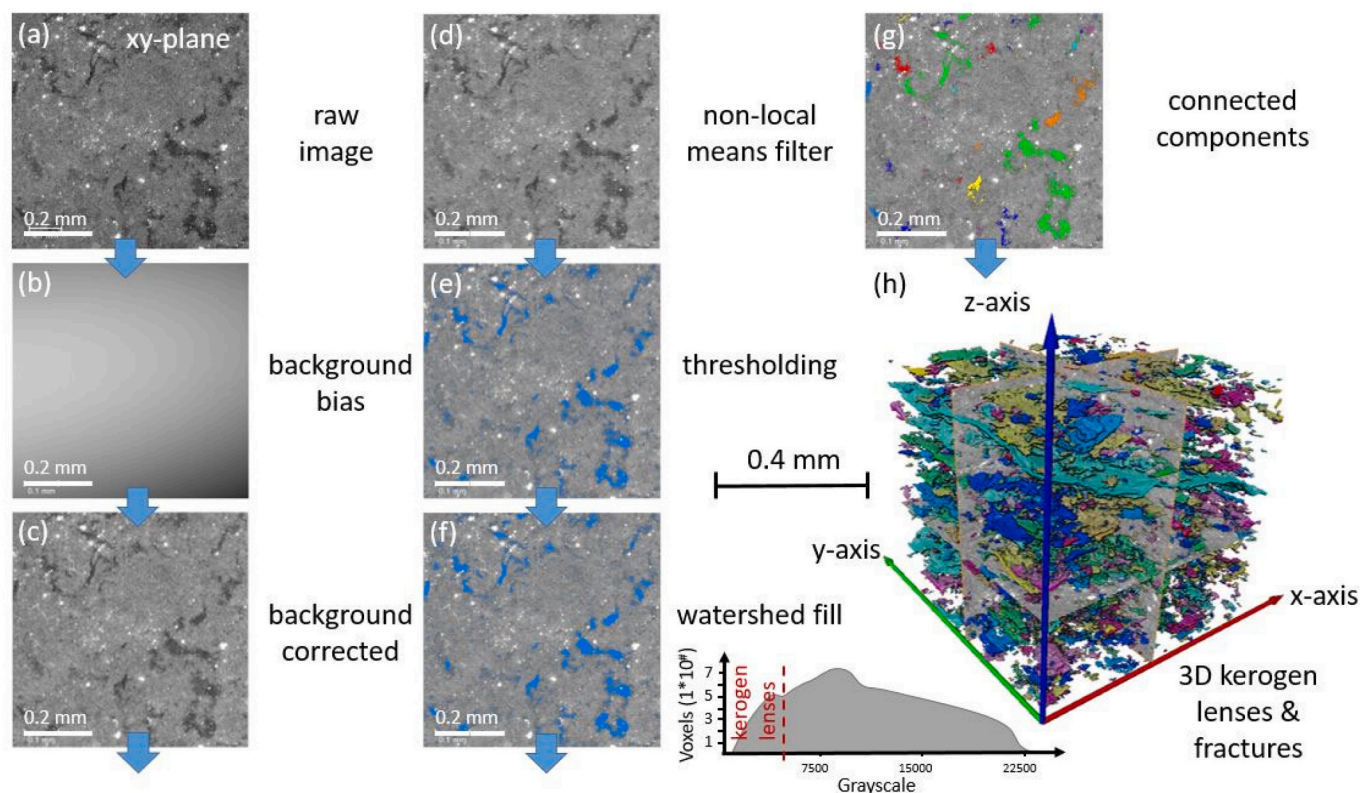
Fig. 2. Three-dimensional synchrotron X-ray microtomography imaging workflow (sample D-2575, 0.7 μm voxel size, 16 bits). (a) Raw initial X-ray phase-contrast image. (b) Background bias is identified and then (c) removed to obtain a background-corrected image. (d) Then, the image is denoised with a non-local means filter. (e) Simple thresholding is applied to separate kerogen lenses and fractures from the rock matrix. (f) Then, a watershed filling procedure is utilized to capture every kerogen lens and microfracture. (g) Image segmentation is followed by separating the data into kerogen lenses and fractures, respectively, by identifying components connected in three dimensions. (h) Volume rendering of the shale sample, the kerogen lenses, and the fractures. The grayscale histogram of the shale volume and the threshold used to segment the kerogen lenses and fractures is displayed.

where the variable x is one of the kerogen lens shape parameters (Eq. 2), B is a normalization constant in order to ensure that the total value of α and β sum to 1. The values of α and β quantify the similarity of curve shapes. If the curve shapes are similar, then the data distribution under those curves is also similar.

3.2. Scanning electron microscopy (SEM) imaging

We have prepared thin sections of the six shale samples in the directions parallel and perpendicular to the natural shale lamination (plane and section views, respectively). The thin sections were coated with carbon and imaged using a Hitachi SU5000 field emission scanning electron microscope, with Electron Dispersive Spectroscopy (EDS) detector, at an acceleration voltage of 15 kV, at the University of Oslo. The images collected cover a range of surface areas. The largest image has a surface area of 3.0×2.25 mm^2, while the smallest image has a surface area of $\sim 0.01 \times 0.007$ mm^2 (Fig. 5).

To quantify the size, shape, and distribution of kerogen lenses on the SEM images, we performed image analysis using the image processing software AvizoFire. Because both epoxy glue and kerogen lenses appear black in SEM images, we separated kerogen from epoxy by chemical composition using EDS data.

The image analysis workflow consists of the following steps: denoising, thresholding, and segmentation (Fig. 6). A non-local means filter was applied to denoise the original grayscale SEM image (Buades et al., 2011). Then, we separated the organic content from the surrounding non-organic minerals. This was done by selecting a greyscale threshold that is unique to the phase of interest (Ketcham, 2005). After this segmentation step, we assigned to each kerogen lens a number

(label), indicated by a set number of colors (Fig. 6d).

We quantitatively characterized the size distribution, shape, smoothness, and dominant direction of the kerogen lenses using the same techniques we applied for the microtomography data (Section 3.1). We calculated the two-dimensional inertia matrix of each kerogen lens. The dominant direction of the kerogen lens was defined by the direction of the largest eigenvector of the inertia matrix and is given by the angle θ relative to the x-axis of the 2D scanning electron microscopy image (Fig. 4b).

$$\mathbf{M_{2D}} = \begin{vmatrix} M_{xx} & M_{xy} \\ M_{xy} & M_{yy} \end{vmatrix} \tag{4}$$

In two-dimensions, the flatness parameter is not defined, and we calculated the 2D anisotropy and elongation parameters as follows:

$$A_{2D} = 1 - \frac{\lambda_3}{\lambda_1}; E_{2D} = \frac{\lambda_2}{\lambda_1} \tag{5}$$

We also quantified the roughness of the kerogen lenses by using the rugosity parameter, Ru, defined by Hamblin and Stachowiak (1995). This parameter quantifies the smoothness of a particle's edges based on the projected particles boundaries as triangles on many scales. Its values are between 0 for a circle and 1 for a highly 'spiky' shape (Hamblin and Stachowiak, 1995). The calculation of this parameter involves measuring the height and sharpness of all convex triangles. This step produces a multi-scale measure of particle spikiness utilized to describe the smoothness of kerogen lenses.

Finally, we used the segmented images (Fig. 6d) to calculate the areal percentage (a. %) of kerogen. We selected only images with surface areas in the range 0.6×0.45 to 3.0×2.25 mm^2 to ensure that a
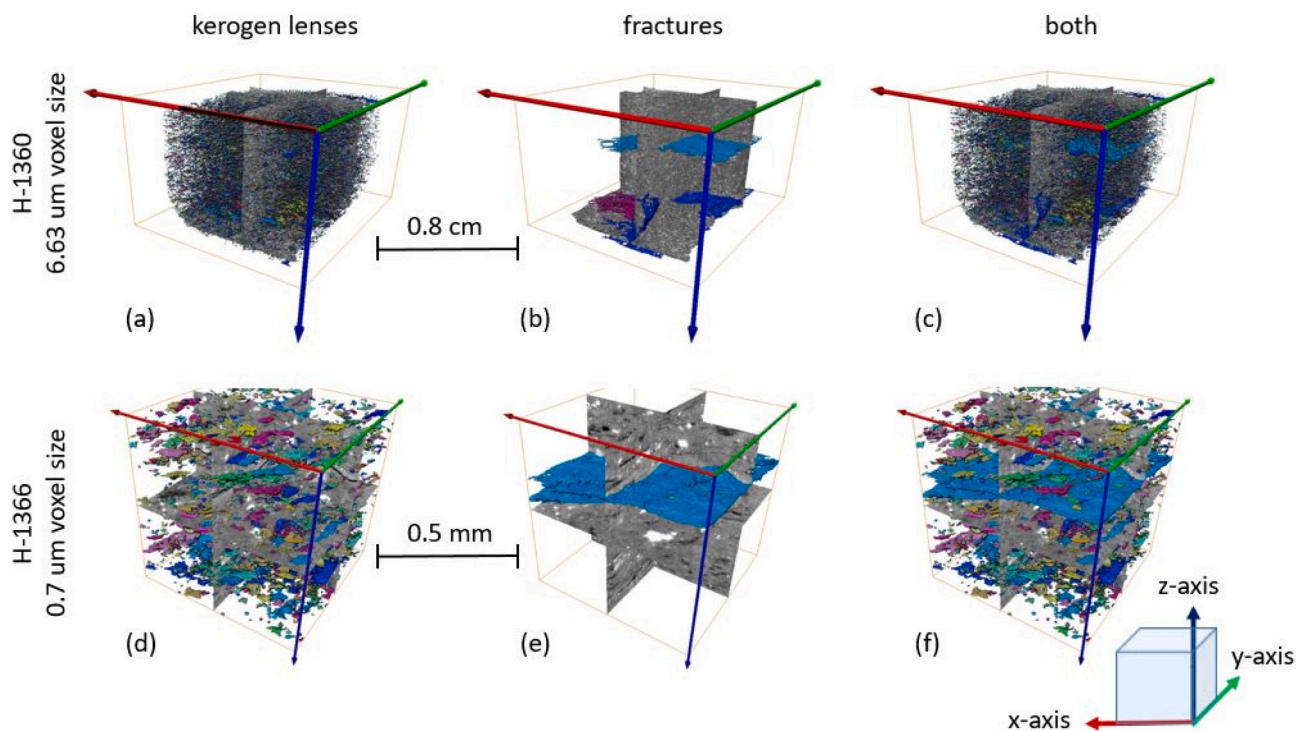
Fig. 3. Three-dimensional rendering views of two shale samples, H-1362, and H-1366. Sample H-1362 is shown at the 6.63 um voxel size, with H-1366 shown at the 0.7 um voxel size. Panels (a) and (d) display the kerogen lenses, panels (b) and (e) display the fractures, and panels (c) and (f) show both kerogen lenses and fractures. The axes are indicated, and the z-axis is perpendicular to sedimentary bedding. Most fractures are parallel to bedding, except one fracture in (b) that also contains a vertical plane (dark blue). (For interpretation of the references to colour in this figure legend, the reader is referred to the web version of this article.)
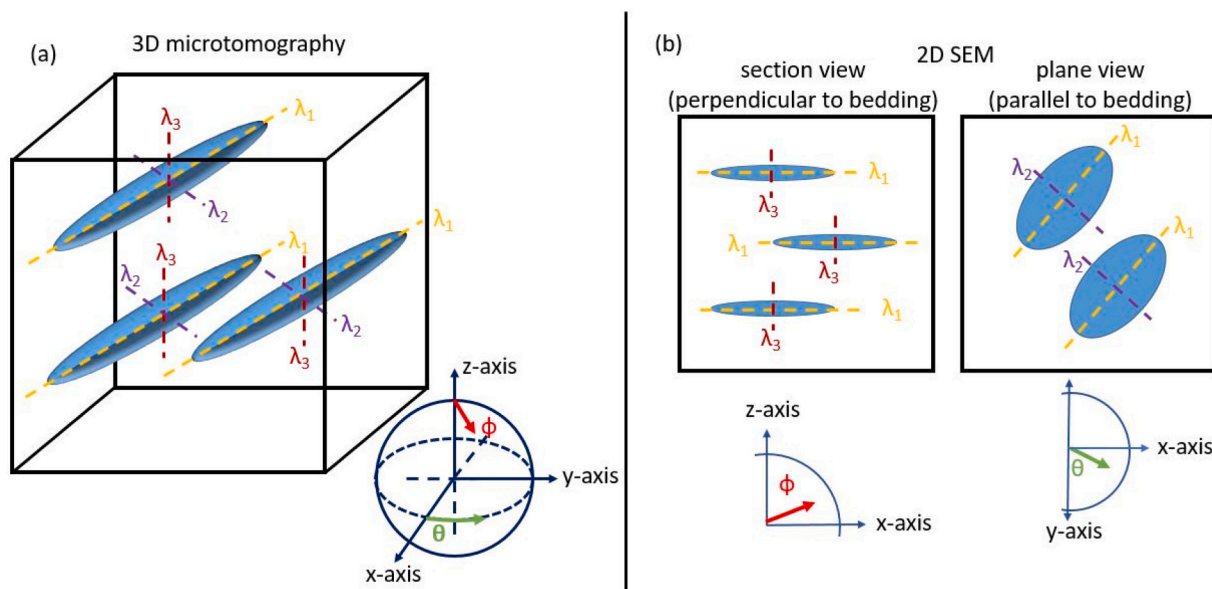

Fig. 4. Sketch showing the eigenvalues of kerogen lenses calculated from the inertia matrix ($\lambda_1 > \lambda_2 > \lambda_3$) and the orientation parameters (θ, φ) for (a) the 3D microtomography data and (b) the 2D scanning electron microscopy data. For the 2D SEM images, we call section view a thin section cut perpendicular to bedding and plane view a thin section cut parallel to bedding.

sufficiently large number of kerogen lenses is present on the image such that the areal percentage calculated is representative of the kerogen content in the shale.

3.3. Geochemical and mineralogical composition

The mineralogical composition of the Draupne and Hekkingen

Formations has been characterized in previous studies (Skurtveit et al., 2015; Nooraiepour et al., 2017; Zadeh et al., 2017; Kalani, 2018; Hansen et al., 2020; Johnson et al., 2021), and is confirmed here. Mineralogy of the samples was measured using X-ray diffraction and confirmed on SEM images of the thin sections (Table 1). Density was calculated for every sample using the weight and volume of the core samples used for 3D microtomography imaging and compared to the well log data. Total
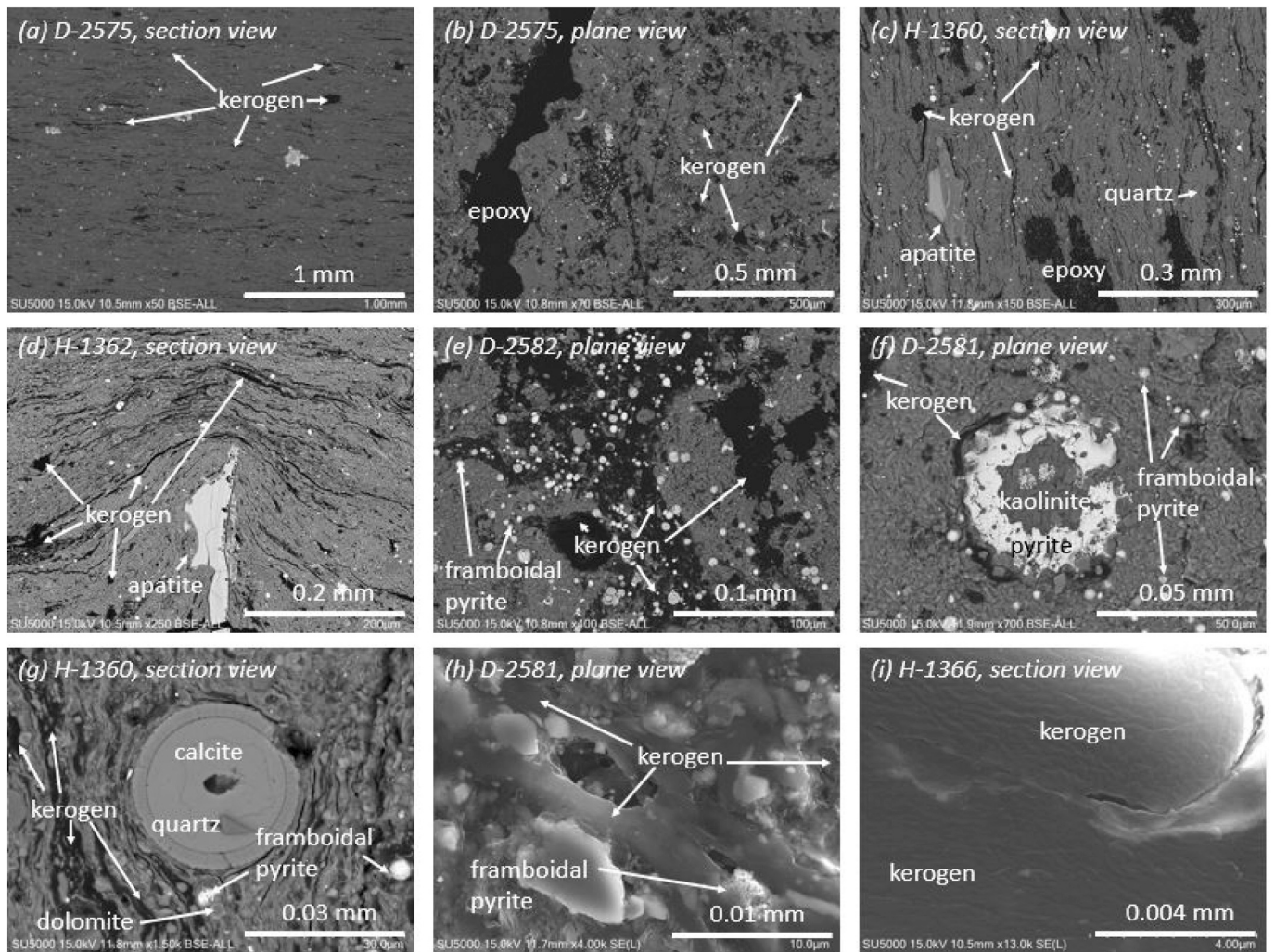
Fig. 5. Scanning electron microscopy images of the studied shale samples. (a) Sample D-2575 in section view (perpendicular to bedding). (b) Sample D-2575 in plane view (parallel to bedding). (c) Sample H-1360 in section view. (d) Sample H-1362 in section view. (e) Sample D-2582 in plane view. (f) Sample D-2581 in plane view. (g) Sample H-1360 in plane view. (h) Sample D-2581 in plane view. (i) Sample H-1366 in section view. See Fig. 4 for the definition of section and plane views.

organic content of the shale samples were taken from Rock-Eval data provided by the Norwegian Petroleum Directorate (NPD, 2021). The typical method of pyrolysis was used on cores/cuttings to determine total organic contents. Well log values of total organic content were calculated using the method of Schmoker and Hester (1983) due to the availability of well logs.

Using SEM data, the amount of organic content was derived by ascertaining the kerogen content within any given image and then accounting for how much of the total area it represented. Similarly, for the 3D microtomography data, the amount of organic content was determined by first identifying all the kerogen lenses and then accounting for how much of the total volume they represented. This calculation was performed at the two spatial sampling distances, 6.63 μm /voxel and 0.7 μm /voxel.

In order to make the comparison between the geochemical and petrophysical calculations of total organic content with total organic content derived from the SEM images and 3D microtomography data, the later total organic content measurement was converted from areal (a. %) or volume percentage (v. %) of the total to a weight percentage (wt%). The following conversion formulas were used:

$$W_{sample} = V_{sample} \times \rho_{sample} \qquad (6)$$

where W_{sample} is the weight of the sample from laboratory

measurements, V_{sample} is the volume of the sample used for 3D microtomography imaging, and ρ_{sample} can be derived from the previous two measurements. In addition,

$$W_{kerogen} = V_{kerogen} \times \rho_{kerogen} \qquad (7)$$

where $W_{kerogen}$ is the weight of the kerogen calculated, $V_{kerogen}$ is the volume of the kerogen calculated from 3D microtomography, and $\rho_{kerogen}$ is 1.25 g/cm^3. Because it was not possible to obtain the density of each kerogen lens, we use here a kerogen density representative for an average of Type II and Type II-S kerogens from the region (Okiongbo et al., 2005), and

$$TOC_{sample} = \frac{W_{kerogen}}{W_{sample}} \qquad (8)$$

where TOC_{sample} (wt%) is the total organic content derived from the ratio between W_{sample} and $W_{kerogen}$, as calculated in Eqs. 6 and 7.

4. Results

4.1. Fracture shape and size

The samples contain fractures that may have formed during decompaction after samples were recovered from depth. Here, we
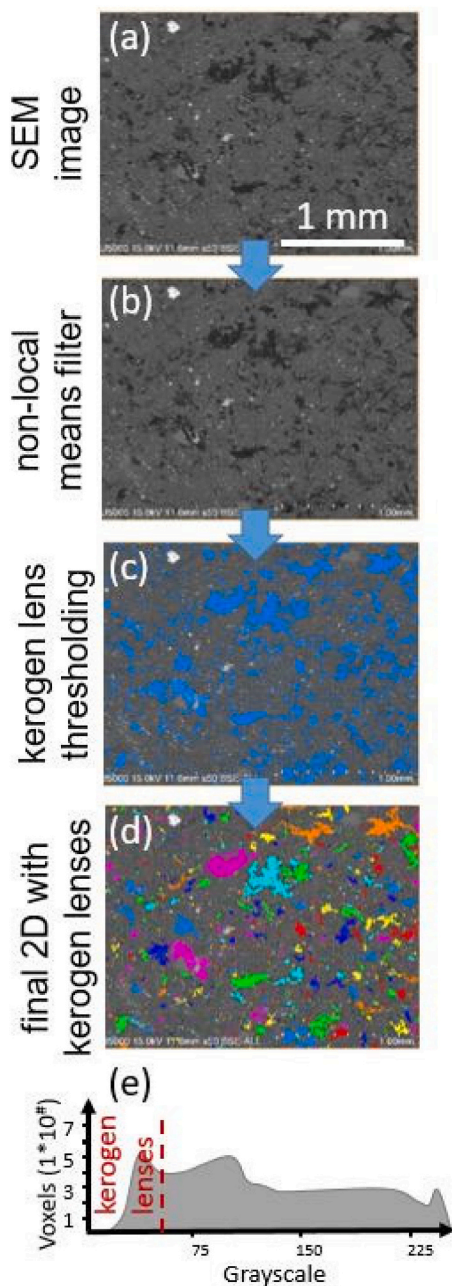
Fig. 6. Data segmentation of SEM images including the (a) original SEM image where we applied (b) a non-local means filter, (c) thresholding in order to select the kerogen lenses, and (d) image segmentation separating out each individual lens. (e) The grayscale histogram indicating the cutoff for separating the kerogen lenses from the rest of the image is indicated.

consider that a microfracture is a single entity of connected voxels, but it could have been formed by merging smaller microfractures with slightly different orientations. We characterize microfractures and their microstructural relationships with kerogen lenses. Fig. 3 shows a three-dimensional rendering of the kerogen lenses and fractures in two samples from the Hekkingen Formation (H-1360, H-1366). The number of fractures varied in each sample (3–13 fractures/sample), with three fractures present in sample H-1362 (Fig. 3b). All of the fractures are mainly horizontal except for one fracture in sample H-1362 (dark blue in Fig. 3b) that contains both horizontal and vertical planes. Most fractures are only found at the 6.63 μm /voxel sampling distance. However, two samples, D-2575 (Fig. 7) and H-1366 (Fig. 3e), contain fractures that can be seen in the 0.7 μm voxel size images.

The interactions between kerogen lenses and fractures can be seen in Fig. 7. A microfracture may intersect several kerogen lenses along its path. However, the total number of kerogen lenses that are in direct contact with fractures is relatively small. The kerogen lenses interact with both the top and bottom of the fracture with an angle of approximately 15 degrees, and in multiple instances, the fracture pathway changes orientation nearby a kerogen lens (Fig. 7). Since these kerogen lenses were connected to the fracture in the 3D tomography data, it was not possible to separate the two. However, the number of kerogen lenses removed in this process was very small (<0.01%), and we consider the impact of this effect on the kerogen statistics presented below very low.

In the six samples scanned at low resolution, we detected a total of 32 microfractures. Only two high-resolution scans contain fractures. The shape parameters of the fractures (Table 2) indicate that fracture length is significantly greater than aperture, with average values F = 0.997 and A = 0.003, respectively. Elongation provided a range of values distributed between 0 and 1, with 17 of the 32 fractures in the range 0.4–0.6 (Table 2). This result indicates that the microfractures have a more or less isotropic shape in their main plane. Together, these data show that microfractures have a penny shape, with an aperture around two orders of magnitude smaller than their length. All fracture planes, except one, are oriented within 25 degrees of bedding. Inside of this category, 17 microfractures were within 10 degrees, and 29 were within 20 degrees. This result indicates that microfracture orientations do not deviate significantly from bedding within our samples.

4.2. Kerogen lens shape and orientation

Fig. 8 shows a three-dimensional rendering of three representative kerogen lenses. The kerogen lenses often do not conform to a typical 'penny-shape' used in numerical models (e.g. Jin et al., 2010; Chauve et al., 2020). Instead, the kerogen lenses occur with a wide variety of shapes and forms. This range in shapes is most apparent in plane-view (XY-plane), where there is a smaller difference in axis size, leading to a larger variety in possible aspect ratios affecting their final form (Fig. 8a). The lens ID #974 from sample H-1360 has a typical penny-shape (Fig. 8). However, in contrast to the typical penny-shape, lens ID# 5292 in sample D-2582 has a tear drop shape, while lens ID # 2697 in sample D-2575 is almost lenticular (Fig. 8). While most kerogen lenses can clearly be described by a compact volume, some lenses appear to be a patchwork of many connected lenses. Another feature of the individual kerogen lenses is the presence of holes that penetrate a certain portion of them (Fig. 8a and c, sample H-1360, lens ID#974).

The shape of all kerogen lenses were also quantitatively analyzed in both plane and section views (Table 3, Fig. 9). In section view, the anisotropy and flatness can be calculated in this reference frame, while the elongation applies to plane-view. In samples scanned at 6.63 um/voxel we identified around 10^4 lenses per sample. In samples scanned at 0.7 um/voxel, we identified around 10^3 lenses per sample. Anisotropy and flatness parameters for all samples are asymmetrically skewed towards higher levels of anisotropy between axis lengths (Table 3, Fig. 9). The skewness is the largest for the anisotropy parameter, with almost all data for the high-resolution scans with values around 0.7, and almost all data for the low resolution scans with values above 0.85 (Table 3, Fig. 9). The flatness parameter shows a broad distribution with almost all data between 0 and 0.8 for the high-resolution scans and almost all data between 0 and 0.4 for the low-resolution scans (Table 3). As the elongation parameter explores plane view, both the total distribution is larger, and the position of the peak is more centered. For elongation, the range of values are within 0.21–0.28 (Table 3). As the dataset size increases, the peak position shifts towards ~0.2 from ~0.3 (Table 3, Fig. 9). The relatively low peak position value indicates that kerogen lenses have a tendency towards an asymmetrical shape (Table 3, Fig. 9). Although, the broad distribution also shows that lenses approaching symmetry are also relatively commonplace.

In our dataset, all of the α and β values across different image
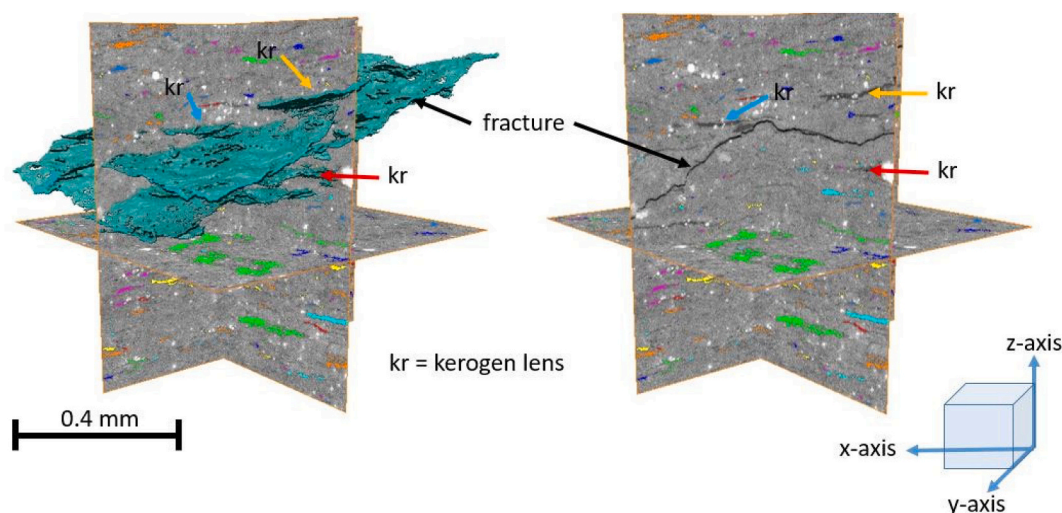
Fig. 7. a) View of sample D-2575 at 0.7 um voxel size showing the presence of kerogen lenses (kr) attached to a fracture. b) Same as panel a) without the 3D rendering of the fracture.

Table 2
Mean values of anisotropy, flatness, elongation, and orientation, φ, for the 32 fractures identified in the six samples. For the anisotropy, flatness, and elongation, the value is in the range 0–1, and the relative proportion in each class (i.e quartile) is given.

Parameters	Average mean	Class (0.00–0.25)	Class (0.25–0.50)	Class (0.50–0.75)	Class (0.75–1.00)
Anisotropy, A	0.003	100%	0%	0%	0%
Flatness, F	0.997	0%	0%	0%	100%
Elongation, E	0.47	21.9%	37.5%	25.0%	15.6%
Orientation, φ	10.6°	–	–	–	–

resolutions are very close (Table 3). The fact that α and β values are similar to one another quantitatively shows that the statistical comparisons between 3D and 2D data hold and are valid.

We utilize the orientation parameters φ and θ to investigate whether kerogen lenses have a dominant alignment direction with their longest principle axis (λ_1). Qualitatively, the high-resolution tomography data from sample H-1366 (Fig. 3d and f) indicate that kerogen lenses have a similar alignment to one another along the y-axis.

The kerogen lenses orientation is represented in Fig. 10 for both microtomography and SEM data. The longest axis of the lenses is oriented close to 90° from the vertical direction, indicating that the main plane of kerogen lenses is oriented parallel to bedding (Fig. 10 a, b). The largest deviation for φ for both the high and low resolutions data is 30 degrees from the bedding plane. Thus, the data at both resolutions show an alignment between the main plane of kerogen lenses and bedding plane, with a rapidly diminishing number of lenses that deviate from bedding (Fig. 10 a, b).

In the bedding plane (plane view in Fig. 10 c, d), the lenses for different samples are oriented along with various directions. This result comes from the sampling because core samples were not oriented when extracted from the boreholes. The total range of angles θ varies between samples. For example, a trend of kerogen lenses directions is measured within the range 165–330 degrees for sample H-1366 (Fig. 10c). However, the same trend can also be relatively confined in a smaller angular range; for example, samples D-2575 and D-2582 both show a 45 degrees dominant trend. Similarly, for the 0.7 μm /voxel data, the dominant directional trends range from 45 to 60 degrees for all samples (Fig. 10).

To summarize, these data show that the kerogen lenses are flat objects whose longest axes are oriented along the bedding plane and that in this plane, the orientation of these lenses has weak directionality.

4.3. Kerogen lens size distribution from synchrotron microtomography data

The segmented tomography images were used to quantify the distribution of sizes of kerogen lenses. Using the spatial coordinates of the center of mass of each kerogen lens in high-resolution images, Fig. 11 displays the distribution of the centers of mass of all of the kerogen lenses in the X-Z and Y-Z planes (perpendicular to bedding) along the X- and Y-axis, and in the XY plane (parallel to bedding) along the Z-axis. The two components perpendicular to bedding show similar curve trends and standard deviations (Fig. 11b, c). This observation suggests a fairly uniform and random distribution of kerogen lenses along the bedding laminations. Along the Z-axis (Fig. 11a), fluctuations in the positions of the centers of mass are larger, suggesting the distribution of kerogen lenses in the direction perpendicular to the lamination is more heterogeneous than along bedding.

One can also differentiate two groups of shales based on total organic carbon (TOC wt%) content and the centre of mass results. The two Hekkingen samples contain above 12 wt% total organic content according to Rock-Eval data, and the remaining four samples contain between 6 and 8 wt% total organic content (Table 4, Fig. 11). Higher values of total organic content correlate with lower total counts of separate kerogen lenses. This inverse relationship suggests that the volume of kerogen lenses in the samples with higher TOC (i.e., H-1362 and H-1366) are greater than for samples with the lower TOC.

Fig. 12a shows the distribution of kerogen lens volumes in relation to the total count in a normalized probability distribution function on a logarithmic scale. Kerogen lenses with volumes between 1×10^{-16} and 5×10^{-13} m^3 are taken from the high-resolution tomography images with 0.7 μm /voxel. Kerogen lenses with volumes between 2×10^{-13} to 7×10^{-10} m^3 are taken from the low-resolution images with 6.63 μm /voxel. The kerogen lens volumes of these two datasets overlap in the range 9×10^{-14} to 1×10^{-12} m^3, as shown by the bounding orange dashed
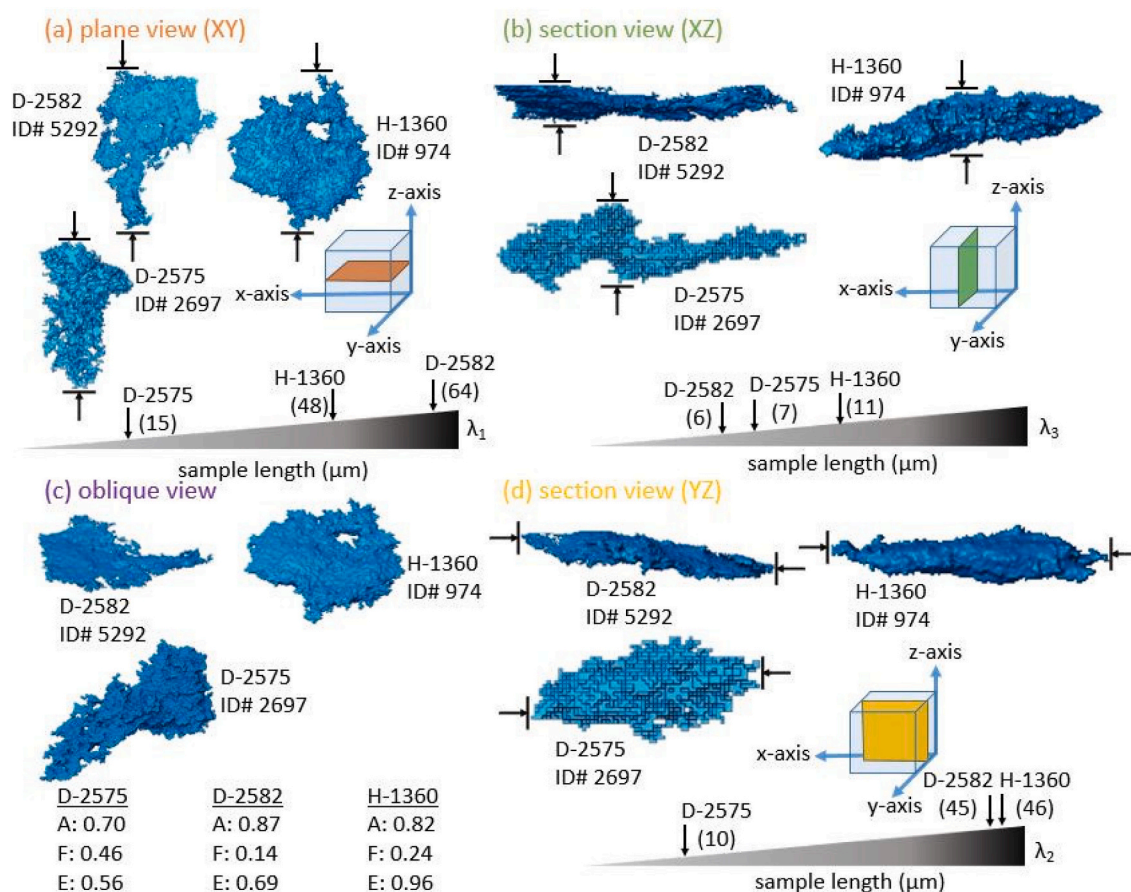
Fig. 8. Three-dimensional rendering of three representative kerogen lenses in samples D-2582 (lens ID# 5292), H-1360 (lens ID# 974), and D-2575 (lens ID# 2697) in (a) plane view, XY-plane (b) section view, XZ-plane (c) oblique view, askew of the XY-plane and (d) section view, YZ-plane. Sample lengths for λ_1, λ_2, and λ_3 are given on scale bars where units are given in micrometers. The anisotropy (A), flatness (F), and elongation (E) values for each kerogen lens are given (bottom left corner), and the eigenvalues of each lens are displayed.

Table 3
Peak position and areas under the asymmetrical curves described by curve shape parameters α and β (Fig. 9) for the anisotropy, flatness, and elongation in both 2D and 3D. Bold numbers indicate the quartile with the greatest percentage of kerogen lenses (% Values).

Data & parameter	Position of the peak	α	β	% Values (0.00–0.25)	% Values (0.25–0.50)	% Values (0.50–0.75)	% Values (0.75–1.00)
0.7 μm / voxel, anisotropy (A_{3D})	0.97	11.83	1.33	0.0	0.5	6.3	**93.3**
6.63 μm / voxel, anisotropy (A_{3D})	0.99	12.28	0.49	0.1	0.3	1.1	**98.5**
0.7 μm / voxel, flatness (F_{3D})	0.15	1.36	3.45	**54.2**	31.5	11.6	2.6
6.63 μm / voxel, flatness (F_{3D})	0.10	0.84	4.22	**78.8**	14.5	5.3	1.4
SEM anisotropy (A_{2D})	0.88	3.31	1.74	4.3	17.5	38.3	**39.9**
0.7 μm / voxel, elongation (E_{3D})	0.21	2.02	3.14	29.3	**43.4**	22.0	5.3
6.63 μm / voxel, elongation (E_{3D})	0.26	2.58	3.14	35.8	**40.0**	18.9	5.3
SEM, elongation (E_{2D})	0.29	2.29	2.98	27.2	**43.3**	21.4	8.2

lines in Fig. 12a. Kerogen lenses can be separated into three distinct groups within the dataset, depending on volume. Between 1×10^{-16} and 2×10^{-13} m³ (Fig. 12a), one power-law relationship with a slope of 0.7 describes the correlations of the volume distribution of kerogen lenses. At a transition scale, corresponding to kerogen lens volumes of around 2×10^{-13} m³ (Fig. 12a), the slope of the power-law that describes the number of kerogen lenses and their volume changes to a value of 1.1. The break in the slope occurs at 2×10^{-13} m³ (Fig. 12a) inside the overlap zone between the low- and high-resolution datasets. Therefore, we consider that the two power laws observed here do not result from the two different resolutions of the images but represent a physical effect.

Finally, a few large kerogen lenses do not appear to be described by either of these power laws (blue dashed square box in Fig. 12a). Note

that these three groups of kerogen lenses exist for all samples regardless of whether they come from the Draupne or Hekkingen Formations.

A relationship is shown between total organic content (wt%) and total kerogen volume in the high-resolution microtomography images (Fig. 12b). The trend for low-resolution data shows a similar result (Fig. S1). In Fig. 12b, two groups of data can be separated. The first group contains shales with a lower total organic content, ranging from ~6 to 8 wt%, and a higher kerogen lens spatial density within a given rock volume (Fig. 12b, green box). The second group contains shales with a higher total organic content, ranging upwards of 12 wt%, and a lower kerogen lens spatial density (Fig. 12b, red box). Fewer kerogen lenses correlating with a higher total organic content is also supported by Fig. 11, where the samples with higher total organic content contain a smaller number of kerogen lenses per volume unit.
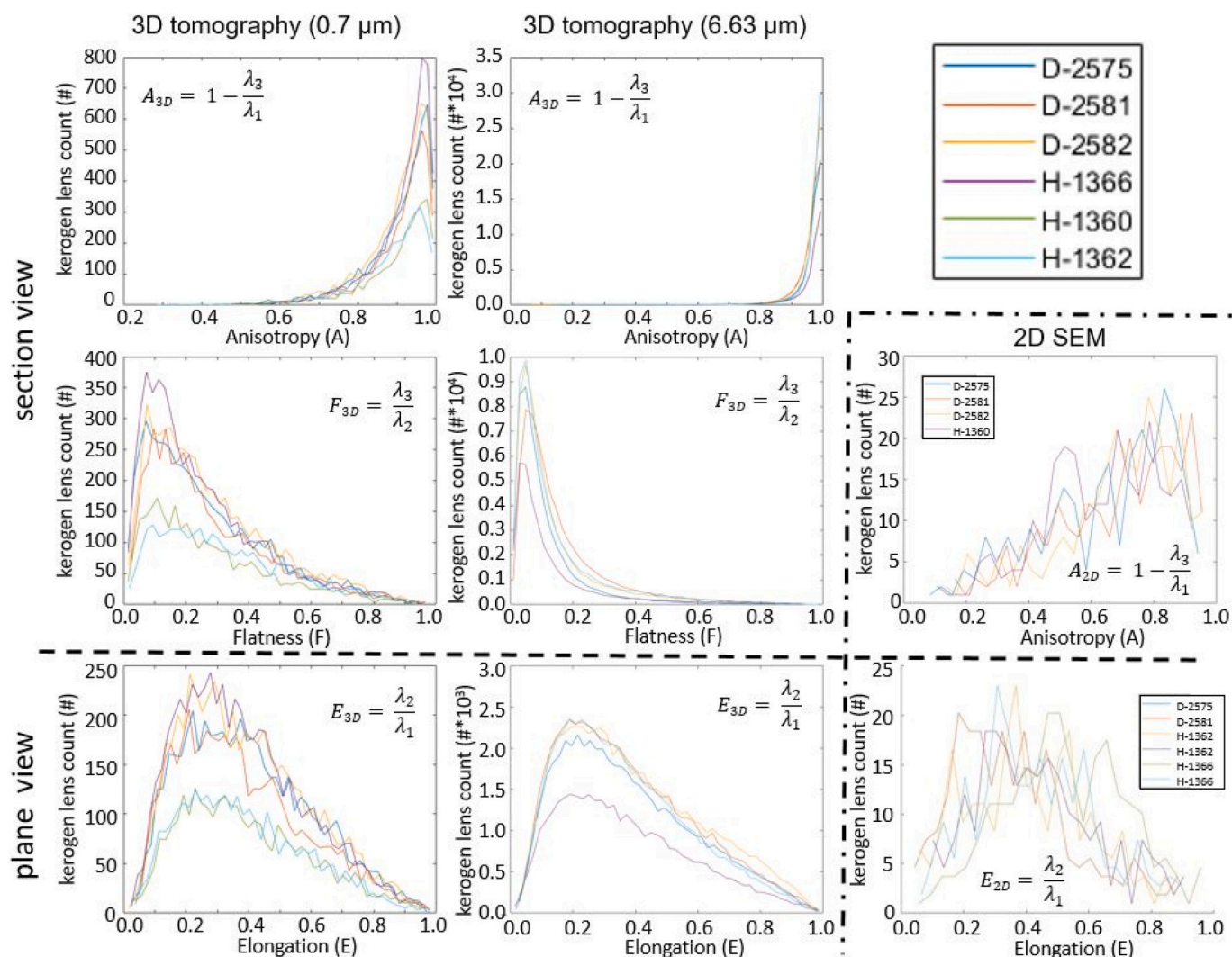
Fig. 9. Probability distribution function both 2D and 3D parameters of anisotropy, flatness, and elongation for synchrotron microtomography data at both high and low resolution, as well as for 0.5–1.0 mm size SEM images. Data are separated into plane and section views, corresponding to parallel and perpendicular orientations to bedding.

Fig. 12c shows the average length of the longest axis of kerogen lenses (λ_1) for both high- and low-resolution microtomography data. A trend can be estimated between the longest axis (λ_1) and total organic content, with an R^2 value of 0.72.

Importantly, the samples with a greater amount of organic matter content also have a longer λ_1 axis. Together, data shown in Figs. 10, 11b, and c suggest that for shales with total organic content in the range 8–12 wt%, organic matter is organized in a smaller number of kerogen lenses that have a longer extension when compared with shales with organic content in the range 5–10%.

4.4. Kerogen lens shape, size, and distribution from SEM data

On SEM images at the 0.5–1 mm scale, the kerogen lenses are often nearly imperceptible in section view (perpendicular to bedding), blending in with the fabric of the shale as a whole, except for a few larger lenses. In plane view (parallel to bedding), the orientation of the lenses allows one to see them more clearly (Figs. 5a, b). In SEM images at higher resolution, kerogen lenses in both the organic-rich Draupne and Hekkingen Formations can be seen in abundance. Fig. 5c and d show soft-sediment deformation around harder fossil clasts and how kerogen lenses follow the fabric of the shale. Fig. 5e, f, and g taken at 0.03–0.1 mm scale show how kerogen lenses interact with the minerals around

them. The kerogen lenses are frequently associated with pyrite, most often framboidal. In this case, pyrite clusters preferentially accumulated in and near the organic matter (Fig. 5e). Coccoliths are abundant in both the Draupne and Hekkingen, and kerogen lenses can be seen conforming to their circular shape (Fig. 5f-g). Using SEM images at higher resolutions, the structure of the kerogen itself at scales less than 0.03 mm is displayed in Fig. 5h and i. Fig. 5h shows a web of kerogen interacting with minerals of the shale matrix. At this scale, some mineral replacement within a kerogen lens can be observed. This mineral replacement may account for the holes seen in some kerogen lenses in the 3D tomography data (Fig. 8, sample H-1360, kerogen lens ID#974). Fig. 5i shows the internal structure of a kerogen lens. The lens has an undular fabric with a dominant direction.

The shape of kerogen lenses is quantified using the aspect ratios of the main axes in 2D (Eqs. 5). The peak position value for the anisotropy parameter of the SEM data is 0.88, which is closer to 3D flatness (F_{3D}) values than 3D anisotropy (A_{3D}) values (Table 3, Fig. 9).

We report the angles φ and θ to investigate whether kerogen lenses have a dominant alignment direction on the longest axis, λ_1. Figs. 2 and 9 show that alignment between kerogen lenses is more apparent in section view than it is in plane view. The angle φ shows a large range of variability, with deviations of +/− 90° (i.e., perpendicular) to the bedding plane (Fig. 10e). However, the majority of deviations occur
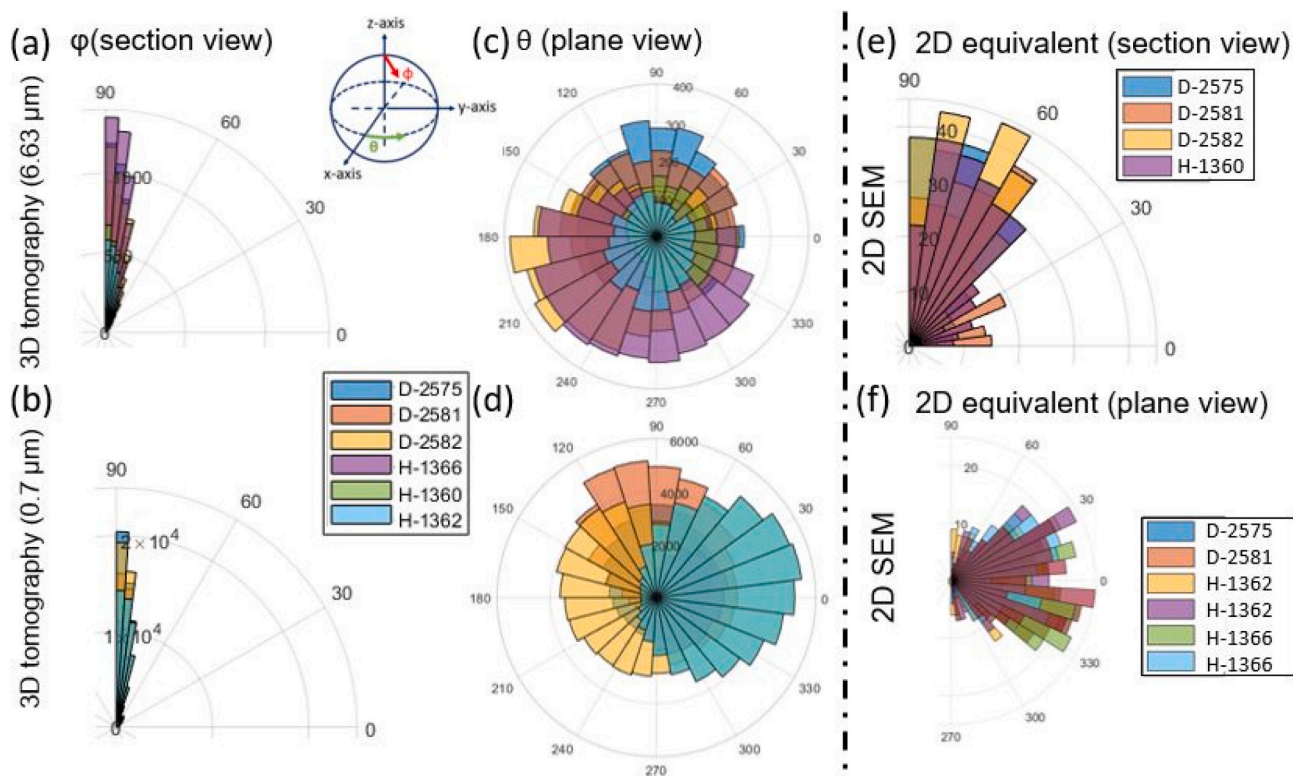
Fig. 10. Rose diagrams showing the orientation angles φ (a, b) and θ (c, d) of kerogen lenses for both high- and low- resolution microtomography data. Rose diagrams show the directions of kerogen lenses for SEM data in both plane and section view (e, f). See inset and Fig. 4 for the definitions of the angles. (For interpretation of the references to colour in this figure legend, the reader is referred to the web version of this article.)

within $+/- 30^o$ of the bedding plane (Fig. 10e). Furthermore, a visual inspection of the section view SEM images reveals that a significant amount of the deviation from the bedding plane is the result of soft-sediment deformation (Fig. 5d and g) around fossils and hard minerals. The angle θ shows that individual samples have kerogen lens orientation within ~15 degrees of one another, while the total data ranges $+/- 30$ degrees for all samples (Fig. 10f). These results suggest a weak directionality of kerogen lenses when they are imaged perpendicular to bedding.

Image analysis from the SEM images of the six samples was used to calculate rugosity, a parameter quantifying the shape of the kerogen lenses. Fig. 13 compares the rugosity of kerogen lenses from SEM images taken at 0.5–1.0 mm scale in both plane (parallel to bedding) and section (perpendicular to bedding) views. The peak value of the rugosity curves is similar for all images, with an average of 0.59 and a standard deviation of 0.1 (Fig. 13). The kerogen lenses have a higher rugosity and therefore are more 'spikey', than reference values for rounded and unrounded quartz grains (Fig. 13).

4.5. Geochemistry and mineralogy

Rock density values calculated from both well data and from the borehole samples are shown in Table 4. The mean rock density from well log analysis is 2.25 g/cm^3 with a standard deviation of 0.08. The mean density from laboratory measurements, calculated from the sample weight and volume from the microtomography data, is 2.28 g/cm^3 with a standard deviation of 0.20. TOC content was estimated using four independent measurements: Rock Eval analysis (pyrolysis), well log analysis (petrophysical analysis), SEM areal analysis, and 3D tomographical volumetric analysis (Table 4). Total organic content values above 2 wt% are considered to be a potential source rock (Kuuskraa et al., 2013; Cooke, 2014). Rock-Eval data show that all six samples have TOC above 6 wt% (Table 4), with Hekkingen samples H-1362 and H-

1366 having TOC above 12 wt%.

Comparisons utilizing all methods show a reasonable agreement between Rock-Eval, well log, and to a lesser degree SEM areal analysis. The TOC values calculated using 3D tomography data are significantly lower than the values collected from Rock-Eval, well log, and SEM. The TOC (wt%) detected for the samples scanned using 3D microtomography at higher resolution was greater than for the same samples scanned at lower resolution. These results indicate that only the largest kerogen lenses were observed at the spatial resolution of the microtomography images. The samples also contain a large number of kerogen lenses with volumes too small to be detected in the 3D images.

Organic-rich shales are complex assemblages of both organic and inorganic components. The inorganic components have a significant impact on the structural integrity of the shale. XRD analyses are used to determine the composition of inorganic components, while SEM is used to the interaction between the organic and inorganic elements. The inorganic material can be classified into three components – stiff quartz and feldspar grains, comparatively soft clay grains, and finally carbonate and pyrite (Fig. 5, Tables 1 and 5). Carbonate and pyrite fractions within the samples are relatively low, with an average of ~10% (Table 5, Fig. S2). Stiffer minerals, quartz, and feldspars, show a significantly greater range for the Draupne and Hekkingen Formations, ranging from 15 to 45% and 20–32%, respectively (Table 5, Fig. S2). Softer clay minerals represent a significant amount in both formations ranging from 40 to 71% for the Draupne Formation, and 58–72% for the Hekkingen Formation (Table 5, Fig. S2). XRD analyses of our samples agree with previous studies within and near our study area (Zadeh et al., 2017; Hansen et al., 2020; Rahman et al., 2020; Johnson et al., 2021).

Clay composition can be classified into four categories: chlorite (< 1% for all samples), kaolinite, smectite, and illite (Fig. 5, Tables 1 and 5, Fig. S2). For both the Draupne and Hekkingen Formations, kaolinite is the dominant clay mineral, with an average of 62.1% and 47%, respectively (Table 5, Fig. S2). The range of kaolinite content is larger
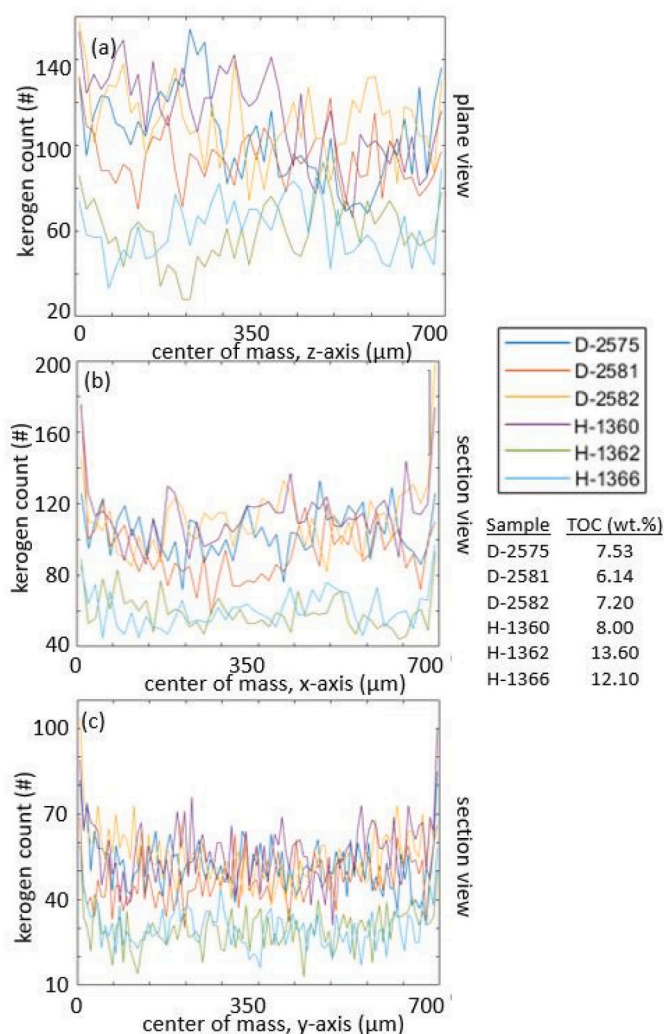
Fig. 11. (a) Number of kerogen lenses versus the centre of mass along the z-axis (plane view, perpendicular to bedding). (b-c) The number of kerogen lenses versus the centre of mass along the x-axis and y-axis (section views, parallel to bedding). For the same rock volume, the two samples with higher total organic content (H-1362, H-1366) contain fewer kerogen lenses.

for the Hekkingen Formation, 46–78%, than for the Draupne Formation, 57–72% (Table 5, Fig. S2). Illite also shows a larger fraction range for the Hekkingen Formation, 14–33%, than for the Draupne Formation, 19–31% (Table 5, Fig. S2). Smectite represents the smallest percentages for both formations. The smectite content in the Hekkingen Formation is

in the range 2–22% and is slightly larger than in the Draupne Formation, where the range is 9–17% (Table 5, Fig. S2).
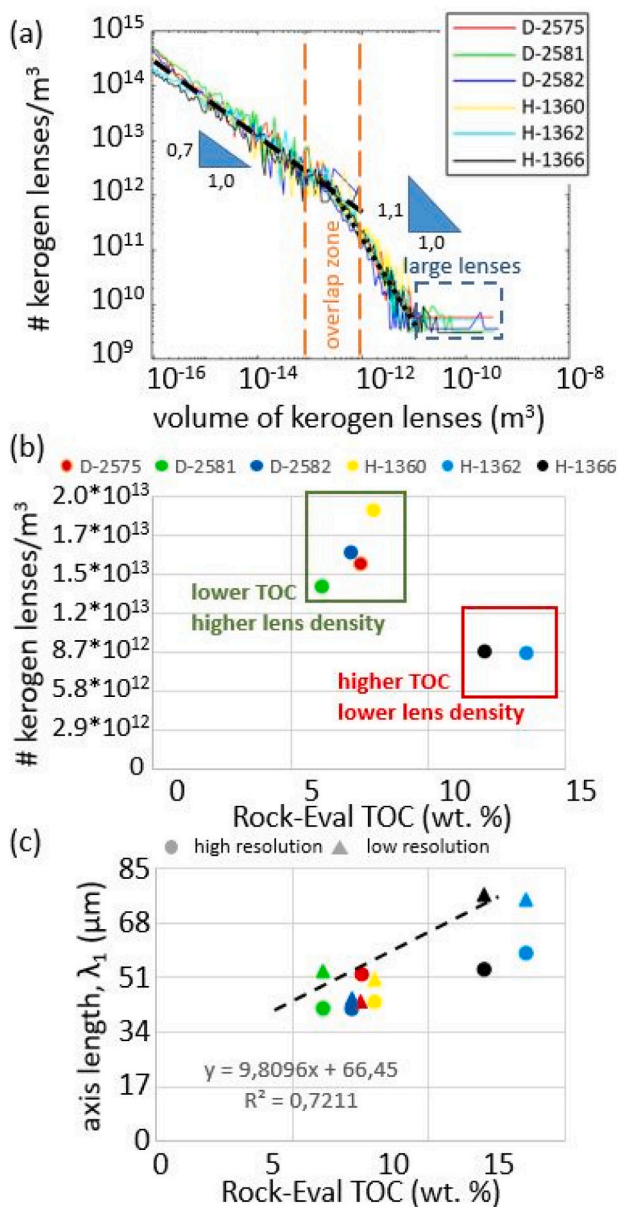
5. Discussion

Kerogen lenses have a direct impact on the microfracturing process during burial and primary migration of hydrocarbon from source rock shales (Kobchenko et al., 2011; Jin et al., 2010; Anders et al., 2014; Chauve et al., 2020). The conversion of kerogen lenses drives microfracturing within shales under appropriate pressure-temperature regimes. The degree of hydrocarbon expulsion and microfractruring (i.e., porosity creation) is influenced by the lithostatic load and modifies the mechanical properties of the rock. While internal kerogen porosity has been documented in some studies (Alfred and Vernik, 2013; Pepper, 2017), our samples do not present any at the resolution of our microscopy images. The present study focuses first on the relationship between the organic and inorganic constituents of organic-rich shale. We quantify the shape, size, and distribution of kerogen lenses based on synchrotron microtomography imaging of six samples collected at different depths in two different organic-rich shale formations in the North Sea and the Barents Sea (dominantly Type II, Type II-S, and Type III kerogen).

5.1. Comparison of techniques – advantages and shortcomings

Investigating the shape of kerogen lenses and TOC in 2D SEM images and 3D microtomography volumes shows significant differences. The two methods are complementary in that SEM imaging can be used to identify mineralogy (Harding, 2002), while 3D microtomography does not yet have this capability unless it is coupled to 3D X-ray diffraction, a technique that was not available on beamline ID19 at ESRF when the samples were imaged. Further to this, certain geological characteristics (i.e., mineral replacement, soft-sediment deformation, etc.) are easier to observe in SEM images than in microtomography volumes. However, 3D microtomography data offer a complete understanding of the organic component of the rock and how it impacts the organic-rich shale as a whole (i.e., fracture-kerogen lens relationship, kerogen lens sizes, and kerogen lens distribution).

Interestingly, SEM areal analyses provide reasonable estimates of TOC compared to other conventional TOC analysis techniques (i.e. Rock-Eval pyrolysis, well log-based TOC estimation). A larger study would be required to confirm repeatability. Conversely, 3D tomography TOC results show that an increase in the spatial resolution correlates to more representative data in terms of TOC because a greater percentage of the total kerogen lenses can be imaged when increasing resolution. The 6.63 μm /voxel data can image on average 5.4% of the organic matter present when utilizing Rock-Eval as a benchmark (Table 4). The 0.7 μm /voxel data can image on average 19.1% of the organic matter present, again compared to Rock-Eval (Table 4). It is likely that the

Table 4
List of samples with density and total organic content (TOC) calculated using different techniques.

Sample	Density well logs (g/cm³)	Density borehole sample (g/cm³)	TOC Rock Eval (wt%)	TOC Well (wt%)	TOC SEM (a. %)	TOC SEM (wt%)	TOC 3D Tomo High Res (v. %)	TOC 3D Tomo Low Res (v. %)	TOC 3D Tomo High Res (wt %)	TOC 3D Tomo Low Res (wt%)
D-2575	2.32	2.39	7.53	6.42	16.4	8.57	2.67	1.00	1.40	0.52
D-2581	2.29	2.12	6.14	5.74	13.3	7.84	2.05	1.15	1.21	0.68
D-2582	2.28	2.23	7.20	5.73	19.0	10.62	2.66	0.48	1.49	0.27
H-1360	2.14	2.21	8.00	7.32	14.5	8.89	2.55	0.89	1.20	0.42
H-1362	2.30	2.66	13.60	12.15	21.3	12.07	4.74	0.67	2.91	0.41
H-1366	2.14	2.04	12.10	11.42	24.6	11.55	4.11	0.49	2.33	0.28

Fig. 12. (a) The probability density function of the volume of kerogen lenses normalized by the sample volume (m³) shows two distinct power-law relationships with slopes 0.7 and 1.1. A group of large kerogen lenses without a clear trend is indicated with a dashed blue box. (b) Number of kerogen lenses per rock volume in high-resolution 3D images (0.7 um/voxel) versus total organic content (wt%). The two boxes separate two class of shale samples. (c) Average longest axis (λ_1) of kerogen lenses versus total organic content (wt%) for high-resolution (circles) and low-resolution (triangles) microtomography data. (For interpretation of the references to colour in this figure legend, the reader is referred to the web version of this article.)

remaining 80.9% would require higher resolution imaging techniques.

5.2. Impact of kerogen lens size, distribution, and shape on primary migration

Kerogen size, distribution, and shape impact the source-rock potential of organic-rich shales. Our study shows a relationship between the spatial distribution and the kerogen lens size (Figs. 12b, c, and 13). Organic-rich shales with TOC of ~12% wt% have larger but ~50% fewer kerogen lenses than shales with TOC between 6 and 8% wt%. The shape of kerogen lenses is classified by aspect ratios given by A_{3D}, F_{3D},
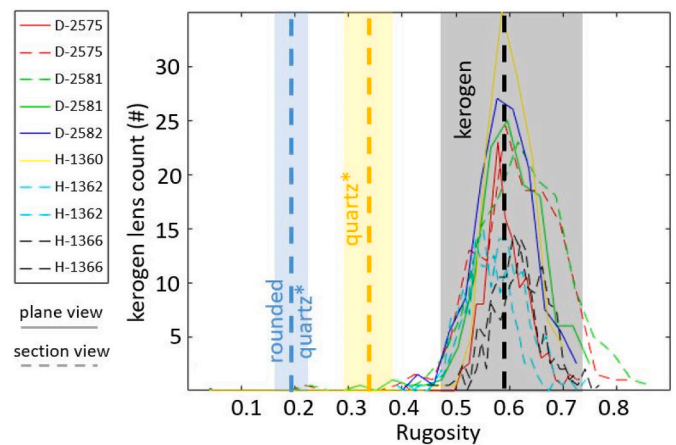
Fig. 13. Shape rugosity of kerogen lenses in 2D calculated from scanning electron microscopy images. Here, rugosity defines the 'spikiness' or roughness of a shape, where a greater value is correlated to a rougher surface. Kerogen lenses are shown to have a rougher surface on average than standard values for quartz and rounded quartz grains (Hamblin and Stachowiak, 1995). Additionally, kerogen lenses show a greater range of roughness values than these minerals. Higher TOC samples show a lower kerogen count (samples H-1362 and H-1366). The mean values of shape roughness are nearly identical for plane views (solid line) and section views (dashed line).

and E_{3D}.

The size and distribution of kerogen lenses play a critical role in microfracture nucleation and growth during hydrocarbon conversion and expulsion. The spatial density of kerogen increases with TOC up to a certain point between 8 and 12% TOC (wt%), above which the kerogen content continues to rise; however, the spatial density of kerogen lenses decreases (Figs. 11, 12, and 13). This effect could be the result of kerogen lenses increasingly combining to form larger kerogen lenses resulting in fewer overall and the production of patchwork lenses (Fig. 14). The 0.7 μm /voxel data captures on average 19.1% of the kerogen lenses present.

To a first-order, linear fracture mechanics indicate that the fluid overpressure required to propagate a fracture, P_p, is inversely proportional to the size of an initial crack (a kerogen lense in our case):

$$P_p \propto \frac{K_c}{\sqrt{\pi * l}} \qquad (9)$$

where K_c is the fracture toughness, and l is the length of the crack. Therefore, larger kerogen lenses may propagate as microfractures under lower fluid pressure. Numerical modeling performed by Fan et al. (2010) showed that kerogen lenses with twice the volume of smaller lenses will propagate faster and farther. Jin et al. (2010) proposed that the development of collinear, subhorizontal cracks connecting kerogen lenses along a given plane plays a role in the pace at which kerogen is converted. Oil pressure decreases exponentially as crack length grows, wherein the full transformation of kerogen to hydrocarbon occurs at the same time that the cracks cease to propagate (Jin et al., 2010; Liu et al., 2021). This effect may control the vertical migration of hydrocarbons, as shales with a complex distribution of kerogen and/or larger kerogen lenses may be more prone to form macroscopic cracks that may connect with pre-existing vertical cracks. Furthermore, the largest kerogen lenses with volume greater than 10^{-11} m³ (Fig. 12a) present in all samples may control the formation of the first and largest microfractures and could have a significant impact on fracture connectivity. Kerogen lens shape and orientation also have an impact on microfracture growth.

The factors that control the shape of kerogen lenses are not fully understood. The final shape is the result of the original biological structure undergoing deposition, degradation, and diagenesis (Farrimond et al., 1998; Farrimond et al., 2002; Vandenbroucke and Largeau,

Table 5

Average bulk and clay mineralogies for the Draupne and Hekkingen from XRD for the study area (Johnson et al., 2021).

Formation	Mineralogy from XRD data					Clay mineralogy			
	Quartz	Feldspar	Pyrite	Carbonate	Total clay	Kaolinite	Smectite	Chlorite	Illite
Draupne shale	22.4	17.8	7.7	1.9	50.7	62.1	18	0.7	19.3
Hekkingen shale	24.2	4.6	5.6	4.5	61	47	20.8	–	32
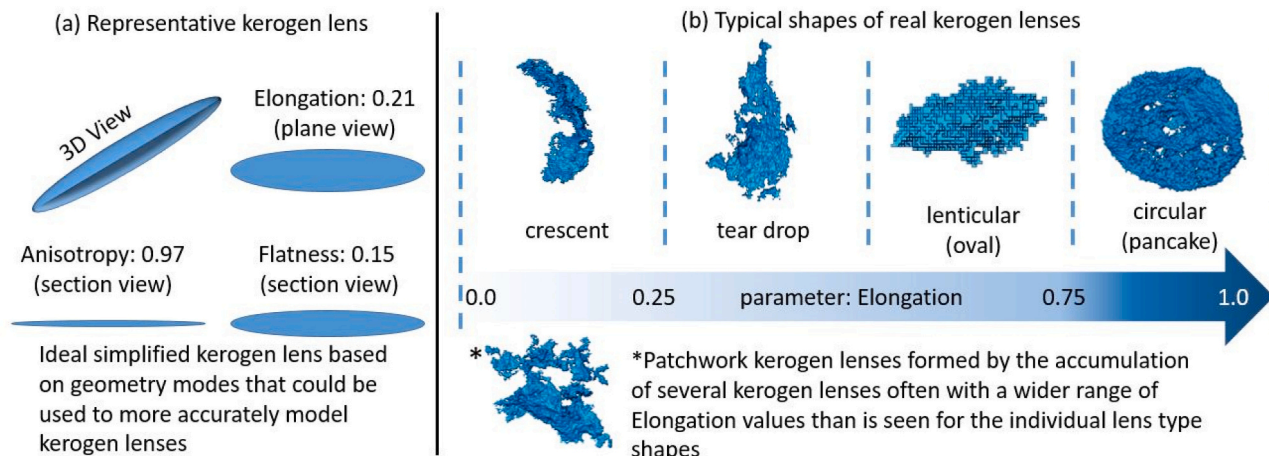
Fig. 14. Shape of kerogen lenses in organic-rich shales. (a) a representative kerogen lens in 3D and cross-section views could be used for better modeling of microfracture nucleation during primary migration. (b) Typical real kerogen lens shapes are classified into five categories. Four of the shapes show aspect ratios based on the elongation parameter: crescent (0.0–0.25), tear drop (0.25–0.5), lenticular (0.5–0.75), and circular (0.75–1.0). Patchwork is another commonly encountered shape that likely resulted from the accumulation of several kerogen lenses.

2007). In our sample, the same basic shapes and forms are present in all samples despite these samples having two distinct well locations with variable geological history. The kerogen here is predominantly Type II and II-S (Johnson et al., 2019; Hansen et al., 2019; Johnson et al., 2021), which supports that shape is influenced by the original biological structures. The erosion due to transport has an impact on the final shape of the organic matter and depends on its pathway to deposition. It is conceivable that Type III kerogen transiting from a terrestrial source will undergo significantly more erosion than Type II kerogen transiting from a marine source. However, the degree to which this process has an impact on the final shape of kerogen lenses remains to be quantified (Huc, 1988; Vandenbroucke and Largeau, 2007). When considering kerogen degradation, studies often refer to changes in the chemical composition of the organic matter, but not how these changes may affect the shape of kerogen lenses (Farrimond et al., 1998; Farrimond et al., 2002; Vandenbroucke and Largeau, 2007). During diagenesis, the interaction between organic and inorganic components may significantly impact kerogen lens shape (Zeszotarski et al., 2004; Prasad et al., 2011; Allan et al., 2014; Zargari et al., 2016). This includes the creation of internal porosity to kerogen lenses (Alfred and Vernik, 2013; Pepper, 2017), followed by the extrusion of bitumen into the created pore space (i.e., microfractures), controlled by lithostatic load.

The consensus is that immature kerogen is a brittle constituent (Brochard et al., 2013; Mondol, 2018; Johnson et al., 2022) that is matrix supporting (Prasad et al., 2011; Allan et al., 2014), and that the dynamic moduli of the lens being dependent on its chemical composition (Alstadt et al., 2016; Bousige et al., 2016). Furthermore, prior to conversion during catagensis, as a result of maturation, kerogen is at its most brittle stage (Zargari et al., 2016). This, in combination with the difference in diagenetic histories between the Draupne and Hekkingen Formations, indicates that if diagenesis plays a significant role in final kerogen shape, it does it during early diagenesis.

Kerogen lenses modelled in the literature (Vernik, 1994; Lash and Engelder, 2005; Fan et al., 2010; Jin et al., 2010; Fan et al., 2012; Chauve et al., 2020; Liu et al., 2021) are lenticular when viewed in section view and circular (penny-shaped) when viewed in plane view. From our data, a representative kerogen lens, based on peak values for anisotropy, flatness, and elongation, is displayed in Fig. 14a.

However, our study also shows that if the dominant shape is lenticular, some variations exist (Fig. 14b). The values of anisotropy and flatness parameterize the variance in aspect ratios that occurs for kerogen lenses in section view (Fig. 9 and Table 3). In plane view, a significant range of kerogen lens shapes exist. Here, we propose to classify the kerogen shapes into five main categories. Four categories are based on the elongation parameter, and the fifth one contains kerogen lenses with patchwork geometry that likely resulted from the coalescence of several smaller lenses (Fig. 14b).

Modeling of fracture propagation within organic-rich shales has been used to propose that the initial direction of the microfracture is guided by the dominant axis alignment of kerogen lenses (Fan et al., 2012; Jia et al., 2018; Chauve et al., 2020). The direction of kerogen lenses is often not perfectly parallel to bedding (Fig. 10), which may have an impact on the early stages of microfracture propagation. As the dominant direction of the lens can vary up to 30° from the bedding plane, it is possible that microfractures initially propagate across bedding, increasing the three-dimensional connectivity of the microfracture network. Further to this, analogue modeling of fracture propagation within shales has shown that fracture can propagate away from areas where stress relief is occurring and continue to propagate in the initial direction of propagation (Kobchenko et al., 2013; Kobchenko et al., 2014; Vega and Kovscek, 2019). This effect could control the growth of some fractures that interact across a wide range of bedding planes, as seen in Fig. 7.

5.3. Impact of mineralogy and total organic content on the sealing properties of shales

The ratio of soft to hard minerals dictates the geomechanical behavior of organic-rich shales under burial temperatures and pressures and, by extension, the sealing behavior of these rocks (Bourg, 2015; Hansen et al., 2020; Rahman et al., 2020; Johnson et al., 2022). Clay

content above 33% within shales dramatically increases sealing capacity (Bourg, 2015), suggesting the Draupne and Hekkingen Formations would have a good sealing property for both hydrocarbons and for geological CO$_2$ sequestration. As proposed by Eliyahu et al. (2015), the shale fabric is influenced by both its organic and inorganic components. Local studies of both the Draupne and Hekkingen shales have indicated that both formations may act as a seal for hydrocarbons (Hansen et al., 2019) and potentially could for CO$_2$ (Rahman et al., 2020). However, because of chemical interactions between CO$_2$/water and clay minerals, it has been proposed that understanding CO$_2$ seals is more complex (Kalani, 2018; Skurtveit et al., 2018). A limited amount of carbonaceous minerals reduces the likelihood of reactivity with CO$_2$ (Busch et al., 2016; Kalani, 2018; Skurtveit et al., 2018), enhancing the potential sealing properties of the Draupne and Hekkingen Formations. However, the amount of smectite present could lead to swell due to CO$_2$ sorption resulting in a stress regime change and ultimately seal failure (Busch et al., 2016).

Comparing the Draupne and Hekkingen Formations, the higher values of smectite and illite with lower average kaolinite content for the Hekkingen Formation (Table 5) suggest it is potentially a better seal (Mondol et al., 2007; Kalani, 2018). However, the Draupne Formation would also objectively be a good seal based on both the overall mineralogy and clay mineralogy, which is supported by other studies within and around the study area (Mondol et al., 2007; Kalani, 2018; Hansen et al., 2020; Rahman et al., 2020; Johnson et al., 2022). Previous studies have shown that higher quantities of organic matter are associated with smectite and illite more than with kaolinite (Ransom et al., 1998; Vandenbroucke and Largeau, 2007). This observation agrees with our results that the Hekkingen Formation has, on average, higher TOC content. One interpretation could be that organic matter has a tendency to adhere around clay particle edges, wherein smectite and illite particles are rougher than kaolinite (Mayer et al., 2004).

Prior to hydrocarbon expulsion, this study confirms the absence of porosity between kerogen lenses and the surrounding minerals at the resolution of our images (Fig. 2). Eliyahu et al. (2015) suggest that porosity would be visible at the nanometer scale in immature kerogen. The large values of kerogen lenses rugosity, or 'spikiness', seen in the 2D SEM images indicate that potential pore-space may have been filled in. Organic-rich shales have the ability to act as a seal after hydrocarbon expulsion, as well as before. Voltolini and Franklin (2020) pointed out that once a fracture network is created, it might not remain open. The ability for organic-rich shales to reseal depends on the ratio of stiff minerals to soft minerals (i.e., clays) (Bourg, 2015; Bourg and Franklin, 2017; Rahman et al., 2020). Soft minerals, such as compressible kaolinite and illite clays, assist the process of shale resealing the most (Bourg and Franklin, 2017). While the Draupne and Hekkingen Formations contain enough kaolinite and illite to assist in resealing, other shales may not. In these cases, kerogen lens shape will also have an impact on sealing capacity after hydrocarbon expulsion. Dietrich (2015) proposed that the pore space left behind from a converted kerogen lens will have an impact on the material properties of the shale. While softer, ductile clay minerals will essentially fill this void space (Voltolini and Franklin, 2020), the stiffer, more brittle minerals will help create porous space within the shale post maturation.

6. Conclusions

Kerogen lens size, distribution, and shape play an important role in determining the properties of organic-rich shales to be the source and seal rocks. We have used multiscale microscopy 2D and 3D imaging techniques to quantify the range of kerogen lens sizes and their frequency of occurrence on six samples collected at depth in boreholes in two locations within the Norwegian North Sea and the Barents Sea. Our study establishes a relationship between the size of kerogen lenses and TOC content wherein an increased TOC content above 12% TOC (wt%) is correlated with an increase in the kerogen lens size and a decrease in

the total number of kerogen lenses per rock volume, for kerogen lenses with a volume larger than the resolution of the images. As a consequence, organic-rich shale with TOC above ~12% contains larger kerogen lenses, whereas organic-rich shales with lower TOC values will contain many more smaller kerogen lenses. Kerogen lenses may provide nucleation sites for microfracture formation during kerogen conversion. Kerogen lenses with a longer extension (TOC > 12%) will fracture under lower fluid pressure than shales with smaller lenses (TOC < 8%). However, shales with a lower TOC may contain many more kerogen lenses and therefore, more nucleation sites to initiate microfractures. There is likely an optimum combination of kerogen lens sizes and spatial density that maximizes damage to the host rock during kerogen maturation.

Our study also provides a range of kerogen lens shapes (Fig. 14) that could be used to model the nucleation and growth of microfractures during primary migration, beyond the simplified penny-shape used in previous numerical studies (Vernik, 1994, Lash and Engelder, 2005; Fan et al., 2010; Jin et al., 2010; Fan et al., 2012; Chauve et al., 2020; Liu et al., 2021). These studies also assume that the tips of kerogen lenses are aligned with the bedding plane, which is not always the case. This assumption also depends on how laminar the rock is, which can be influenced by both deposition (i.e. lacustrine, transition, marine) and diagenesis. The variety of kerogen lens geometries may have an impact on microfracture growth and how microfractures may connect in three dimensions. This microfracture network controls primary migration or the sealing capacities of shales for CO$_2$ or nuclear waste storage in cases where a significant degree of uplift has occurred, as it is the case in the Barents Sea.

Declaration of Competing Interest

The authors declare that they have no known competing financial interests or personal relationships that could have appeared to influence the work reported in this paper.

Appendix A. Supplementary data

Supplementary data to this article can be found online at https://doi.org/10.1016/j.coal.2022.103954.

References

Abay, B.T., 2017. Diversity of Petroleum in Terms of Source Rock Properties and Secondary Alteration Processes. PhD Thesis. University of Oslo.

Alfred, D., Vernik, L., 2013. A new petrophysical model for organic shales. Petrophysics 54 (3), 240–247.

Allan, A.M., Vanorio, T., Dahl, J.E.P., 2014. Pyrolysis-induced P-wave velocity anisotropy in organic-rich shales. Geophysics 79, 41–53. https://doi.org/10.1190/geo2015-0514.1.

Alstadt, K.N., Katti, K.S., Katti, D.R., 2016. Nanoscale morgphology of kerogen and in situ nanomechanical properties of Green River oil shale. J. Nanomech. Micromech. 6, 1. https://doi.org/10.1061/(ASCE)NM.2153-5477.0000103.

Anders, M.H., Laubach, S.E., Scholz, C.H., 2014. Microfractures: a review. J. Struct. Geol. 69, 377–394. https://doi.org/10.1016/j.jsg.2014.05.011.

Avizo Reference Manual, 2021. https://assets.thermofisher.com/TFS-Assets/MSD/Product-Guides/users-guide-avizo-software-2019.pdf.

Baig, I., Faleide, J.I., Jahren, J., Mondol, N.H., 2016. Cenozoic exhumation on the southwestern Barents Shelf: estimates and uncertainties constrained from compaction and thermal maturity analyses. Mar. Pet. Geol. 73, 105–130. https://doi.org/10.1016/j.marpetgeo.2016.02.024.

Baig, I., Faleide, J.I., Mondol, N.H., Jahren, J., 2019. Burial and exhumation history control on shale compaction and thermal maturity along the Norwegian North Sea basin margin areas. Mar. Pet. Geol. 104, 61–85. https://doi.org/10.1016/j.marpetgeo.2019.03.010.

Bourg, I.C., 2015. Sealing Shales versus Brittle Shales: a sharp threshold in the material properties and energy technology uses of fine-grained sedimentary rocks. Environ. Sci. Technol. Lett. 2, 255–259. https://doi.org/10.1021/acs.estlett.5b00233.

Bourg, I.C., Franklin, J.B.A., 2017. Clay, water, and salt: controls on the permeability of fine-grained sedimentary rocks. Acc. Chem. Res. 50, 2067–2074. https://doi.org/10.1021/acs.accounts.7b00261.

Bousige, C., Ghimbeu, C.M., Guterl, C.V., Pomerantz, A.E., Suleimenova, A., Vaughan, G., Garbarino, G., Feygenson, M., Wildgruber, C., Ulm, F.J., Pellenq, R.J.M., Coasne, B., 2016. Realistic molecular model of kerogen's nanostructure. Nat. Mater. 15 https://doi.org/10.1038/NMAT4541.

Brochard, L., Hantal, G., Laubie, H., Ulm, F.J., Pellenq, R.J.M., 2013. Fracture mechanisms in organic-rich shales: role of kerogen. Poromechanics V 2471–2480. https://doi.org/10.1061/9780784412992.288.

Buades, A., Coll, B., Morel, J.M., 2011. Non-local means denoising. Image Process. On Line 1, 208–212. https://doi.org/10.5201/ipol.2011.bcm_nlm.

Burnham, A.K., 2017. Porosity and permeability of Green River oil shale and their changes during retorting. Fuel 2017 (203), 208–213. https://doi.org/10.1016/j.fuel.2017.04.119.

Busch, A., Bertier, P., Gensterblum, Y., Rother, G., Spiers, C.J., Zhang, M., Wentinck, H. M., 2016. On sorption and swelling of CO2 in clays. Geomech. Geophys. Geo-Energy Geo-Resour. 2, 111–130. https://doi.org/10.1007/s40948-016-0024-4.

Carcione, J.M., Avseth, P., 2015. Rock-physics templates for clay-rich source rocks. Geophysics 80 (5), D481–D500. https://doi.org/10.1190/GEO2014-0510.1.

Chauve, T., Scholtès, L., Donzé, F., Mondol, N.H., Renard, F., 2020. Layering in shales controls microfracturing at the onset of primary migration in source rocks. J. Geophys. Res. 125, e2020JB019444 https://doi.org/10.1029/2020JB019444.

Cooke, I.L., 2014. User Guide Total Organic Carbon (TOC) Dataset: British Geological Survey (BGS). Internal Report.

Craddock, P.R., Bake, K.D., Pomerantz, A.E., 2018. Chemical, molecular, and microstructural evolution of kerogen during thermal maturation: case study from the Woodford Shale of Oklahoma. Energy Fuel 32, 4859–4872. https://doi.org/10.1021/acs.energyfuels.8b00189.

Craddock, P.R., Mosse, L., Bernhardt, C., Ortiz, A.C., Tomassini, F.G., Saldungaray, P., Pomerantz, A.E., 2019. Characterization and range of kerogen properties in the Vaca Muerta Formation Neuquen Basin, Argentina. Org. Geochem. 129, 42–44.

Dewhurst, D.N., Siggins, A.F., 2006. Impact of fabric, microcracks and stress field on shale anisotropy. Geophys. J. Int. 165, 135–148. https://doi.org/10.1111/j.1365-246X.2006.02834.x.

Dietrich, A.B., 2015. The Impact of Organic Matter on Geomechanical Properties and Elastic Anisotropy in the Vaca Muerta Shale. M.Sc. Thesis. Colorado School of Mines.

Dore, A.G., Vollset, J., Hamar, G.P., 1985. Correlation of the offshore sequences referred to the Kimmeridge Clay Formation – relevance to the Norwegian sector. Petrol. Geochem. Explor. Norwegian Shelf 1, 27–37. https://doi.org/10.1007/978-94-009-4199-1_2.

Eliyahu, M., Emmanuel, S., Day-Stirrat, R., Macaulay, C.I., 2015. Mechanical properties of organic matter in shales mapped at the nanometer scale. Mar. Pet. Geol. 59, 294–304. https://doi.org/10.1016/j.marpetgeo.2014.09.007.

Faleide, J.I., Tsikalas, F., Breivik, A.J., Mjelde, R., Ritzmann, O., Engen, O., Wilson, J., Eldholm, O., 2008. Structure and evolution of the continental margin off Norway and the Barents Sea. Episodes 31, 82–91. https://doi.org/10.18814/epiiugs/2008/v31i1/012.

Fan, Z.Q., Jin, Z.H., Johnson, S.E., 2010. Subcritical propagation of an oi-filled penny-shaped crack during kerogen-oil conversion. Geophys. J. Int. 182, 1141–1147. https://doi.org/10.1111/j.1365-246X.2010.04689.x.

Fan, Z.Q., Jin, Z.H., Johnson, S.E., 2012. Gas-driven subcritical crack propagation during conversion of oil to gas. Pet. Geosci. 18, 191–199. https://doi.org/10.1144/1354-079311-030.

Farrimond, P., Taylor, A., Telnaes, N., 1998. Biomarker maturity parameters: the role of generation and thermal degradation. Org. Geochem. 29, 1181–1197. https://doi.org/10.1016/S0146-6380(98)00079-5.

Farrimond, P., Griffiths, T., Evdokiadis, E., 2002. Hopanoic acids in Mesozoic sedimentary rocks: their origin and relationship with hopanes. Org. Geochem. 33, 965–977. https://doi.org/10.1016/S0146-6380(02)00059-1.

Hamblin, M.G., Stachowiak, G.W., 1995. A multi-scale measure of particle abrasivity, and its relation to two-body abrasive wear. Wear 190, 190–196. https://doi.org/10.1016/0043-1648(95)06624-1.

Hansen, J.A., Mondol, N.H., Fawad, M., 2019. Organic content and maturation effects on elastic properties of source rock shales in the Central North Sea. Interpretation 7, 477–497. https://doi.org/10.1190/INT-2018-0105.1.

Hansen, J.A., Mondol, N.H., Tsikalas, F., Faleide, J.I., 2020. Caprock characterization of Upper Jurassic organic-rich shales using acoustic properties, Norwegian continental shelf. Mar. Pet. Geol. 121, 104603 https://doi.org/10.1016/j.marpetgeo.2020.104603.

Harding, D.P., 2002. Mineral identification using a scanning electron microscope: Mining. Metall. Explor. 19, 215–219. https://doi.org/10.1007/BF03403272Kal.

Henriksen, E., Bjornseth, H.M., Hals, T.K., Heide, T., Kiryukhina, T., Klovjan, O.S., Larssen, G.B., Ryseth, A.E., Ronning, K., Sollid, K., Stoupakova, A., 2011. Uplift and erosion of the greater Barents Sea: impact on prospectivity and petroleum systems. Geol. Soc. Mem. 35, 1–271. https://doi.org/10.1144/M35.17.

Huc, A.Y., 1988. Aspects of depositional processes of organic matter in sedimentary basins. Org. Geochem. 13, 263–272.

Hunt, J.M., 1996. Petroleum Geochemistry and Geology. Freeman, New York.

Jia, Y., Lu, Y., Tang, J., Fang, Y., Xia, B., Ge, Z., 2018. Mechanical-chemical-mineralogical controls on permeability evolution of shale fractures. Geofluid. https://doi.org/10.1155/2018/7801843.

Jiang, S., Tang, X., Cai, D., Xue, G., He, Z., Long, S., Peng, Y., Gao, B., Xu, Z., Dahdah, N., 2017. Comparison of marine, transitional, and lacustrine shales: a case study from the Sichuan Basin in China. J. Pet. Sci. Eng. 150, 334–347. https://doi.org/10.1016/j.petrol.2016.12.014.

Jin, Z.H., Johnson, S.E., Fan, Z.Q., 2010. Subcritical propagation and coalescence of oil-filled cracks: getting the oil out of low-permeability source rocks. Geophys. Res. Lett. 37, L01305. https://doi.org/10.1029/2009GL041576.

Johnson, J.R., 2017. Applications of Geostatistical Seismic Inversion to the Vaca Muerta, Neuquen Basin, Argentina. M.S. thesis. Colorado School of Mines.

Johnson, J.R., Hansen, J., Renard, F., Mondol, N.H., 2019. Modeling maturation, elastic, and geomechanical properties of the Draupne Formation, offshore Norway. In: 2019 SEG Annual Meeting. SEG.

Johnson, J.R., Renard, F., Mondol, N., 2021. Salt remobilization timing and its impact on two Norwegian Contentinental Shelf organic-rich shale formations. Geoconvention 2021. https://geoconvention.com/wp-content/uploads/abstracts/2021/67503-salt-removilization-timing-and-its-impact-on-two.n.pdf.

Johnson, J.R., Hansen, J.A., Rahman, F., Renard, F., Mondol, N.H., 2022. Mapping the maturity of organic-rich shale with combined geochemical and geophysical data, Draupne Formation, Norwegian Continental Shelf. Mar. Pet. Geol. 138, 105525 https://doi.org/10.1016/j.marpetgeo.2022.105525.

Kalani, M., 2018. Implications from Clay Sedimentology, Well Log Interpretation and Seismic Analyses. PhD Thesis. University of Oslo.

Kelemen, S.R., Walters, C.C., Ertas, D., Kwiatek, L.M., Curry, D.J., 2006. Petroleum expulsion part 2. Organic matter type and maturity effects on Kerogen swelling by solvents and thermodynamic parameters for Kerogen from regular solution theory. Energy Fuel 20, 301–308. https://doi.org/10.1021/ef0580220.

Ketcham, R.A., 2005. Three-dimensional grain fabric measurements using high-resolution X-ray computed tomography. J. Struct. Geol. 27, 1217–1228. https://doi.org/10.1016/j.jsg.2005.02.006.

Kobchenko, M., Panahi, H., Renard, F., Dysthe, D.K., Malthe-Sorenssen, A., Mazzini, A., Scheibert, J., Jamtveit, B., Meakin, P., 2011. 4D imaging of fracturing in organic-rich shales during heating. J. Geophys. Res. 116, B12201. https://doi.org/10.1029/2011JB008565.

Kobchenko, M., Hafver, A., Jettestuen, E., Galland, O., Renard, F., Meakin, P., Jamtveit, B., Dysthe, D., 2013. Drainage fracture networks in elastic solids with internal fluid generation. Lett. J. Explor. Front. Phys. 102, 66002. https://doi.org/10.1209/0295-5075/102/66002.

Kobchenko, M., Hafver, A., Jettestuen, E., Renard, F., Galland, O., Jamtveit, B., Meakin, P., Dysthe, D.K., 2014. Evolution of a fracture network in an elastic medium with internal fluid generation and expulsion. Phys. Rev. 90, 052801 https://doi.org/10.1103/PhysRevE.90.052801.

Kuuskraa, V.A., Stevens, S.H., Moodhe, K., 2013. Technically Recoverable Shale Oil and Shale Gas Resources: An Assessment of 137 Shale Formations in 41 Countries outside the United States. U.S. Energy Information Administration. https://www.eia.gov/analysis/studies/worldshalegas/pdf/overview.pdf?zscb=79906188.

Lash, G.G., Engelder, T., 2005. An analysis of horizontal microcracking during catagenesis: example from the Catskill delta complex. AAPG Bull. 89, 1322–1449. https://doi.org/10.1306/05250504141.

Li, S., Zhang, D., 2021. Development of 3-D curved fracture swarms in shale rock driven by rapid fluid pressure buildup: Insights from numerical modeling. Geophys. Res. Lett. 4, 1–12. https://doi.org/10.1029/2021GL0926338.

Liu, G., Chen, Y., Du, X., Xiao, P., Liao, S., Azzam, R., 2021. Investigation of microcrack propagation and energy evolution in brittle rocks based on the voronoi model. Materials 14, 1–24. https://doi.org/10.3990/ma14092108.

Mayer, L.M., Schick, L.L., Hardy, K.R., Wagal, R., McCarthy, J., 2004. Organic matter in small mesopores in sediments and soil. Geochim. Cosmochim. Acta 68, 3863–3872.

Mittone, A., Manakov, I., Broche, L., Jarnias, C., Coan, P., Bravin, A., 2017. Characterization of a sCMOS-based high-resolution imaging system. J. Synchrotron Radiat. 24 (6), 1226–1236.

Mondol, N.H., 2018. Seal quality prediction using E-Poisson's ratio rock physics template – a case study from the Norwegian Barents Sea. Geoconvention 2018. https://geoconvention.com/uploads/2018abstracts/241_GC2018_Seal_quality_prediction_using_E-v_rock_physics_templet.pdf.

Mondol, N.H., Bjorlykke, K., Jahren, J., Hoeg, K., 2007. Experimental mechanical compaction of clay mineral aggregates – changes in physical properties of mudstones during burial. Mar. Pet. Geol. 24, 289–311. https://doi.org/10.1016/j.marpetgeo.2007.03.006.

Muller, R., Klausen, T.G., Faleide, J.I., Olaussen, S., Eide, C.H., Suslova, A., 2019. Linking regional unconformities in the Barents Sea to compression-induced forebulge uplift at the Triassic-Jurassic transition. Tectonophysics 765, 35–51. https://doi.org/10.1016/j.tecto.2019.04.006.

Nichols, T.C., 1992. Rebound in the Pierre Shale of South Dakota and Colorado – field and laboratory evidence of physical conditions related to processes of shale rebound. In: USGS Report Open-File, pp. 92–440.

Nichols, T.C., Collins, D.S., Davidson, R.R., 1986. In situ and laboratory tests of the Pierre Shale near Hayes, South Dakota – a characterization of engineering behavior. Can. Geotech. J. 23, 181–194. https://doi.org/10.1139/t86-028.

Nooraiepour, M., Mondol, N.H., Hellevang, H., Bjorlykke, K., 2017. Experimental mechanical compaction of reconstituted shale and mudstone aggregates: Investigation of petrophysical and acoustic properties of SW Barents Sea cap rock sequences. Mar. Pet. Geol. 80, 265–292. https://doi.org/10.1016/j.marpetgeo.2016.12.003.

NPD, 2021. Norwegian Petroleum Directorate FactPages. http://factpages.npd.no/ accessed March 27, 2021.

Ohm, S.E., Karlsen, D.A., Austin, T.J.F., 2008. Geochemically driven exploration models in uplifted areas: examples from the Norwegian Barents Sea. AAPG Bull. 92, 1191–1223. https://doi.org/10.1306/0618080808028.

Okewale, I.A., Grobler, H., 2020. Mechanics of compression behaviour in shale. In: 2020 World Congress on Advances in Civil, Environmental, & Materials Research, Seoul, Korea. http://www.i-asem.org/publication_conf/acem20/2.GE/3.General/GE1161_6330F1.pdf.

Okiongbo, K., Aplin, A., Larter, S., 2005. Changes in type II Kerogen density as a function of maturity: evidence from the Kimmeridge clay formation. Energy Fuel 19, 2495–2499.

Panahi, H., Kobchenko, M., Meakin, P., Dysthe, D.K., 2019. Fluid expulsion and microfracturing during the pyrolysis of an organic rich shale. Fuel 235, 1–16. https://doi.org/10.1016/j.fuel.2018.07.069.

Pelet, R., Tissot, B., 1971. Nouvelles Données sur les Mécanismes de Genèse et de Migration du Pétrole Simulation Mathématique et Application à la Prospection. In: 8th World Petroleum Congress, 13–18 June, Moscow, USSR, 12 pgs.

Pepper, A., 2017. Definition, modes of occurrence and pitfalls in understanding the term 'bitumen' in conventional and unconventional petroleum systems. In: 2017 AAPG Convention & Exhibition. https://www.searchanddiscovery.com/documents/2017/42111pepper/ndx_pepper.pdf.

Pepper, A.S., Corvi, P.J., 1995. Simple kinetic models of petroleum formation. Part III: modelling an open system. Mar. Pet. Geol. 12 (4), 417–452. https://doi.org/10.1016/0264-8172(95)96904-5.

Prasad, M., Pal-Bathija, A., Johnston, M., Rydzy, M., Batzle, M., 2009. Rock physics of the unconventional. Lead. Edge 28, 34–38. https://www.mines.edu/crusher/wp-content/uploads/sites/126/2018/03/Publication_Prasad_UnconvRockPhysics_TLE2009.pdf.

Prasad, M., Kenechukwu, C., McEvoy, T.E., Batzle, M., 2011. Maturiy and impedance anlaysis of organic-rich shales. SPE Reserv. Eval. Eng. 14, 533–543. https://doi.org/10.2118/123531-PA.

Rahman, H.M., Kennedy, M., Lohr, S., Dewhurst, D.N., Sherwood, N., Yang, S., Horsfield, B., 2017. The influence of shale depositional fabric on the kinetics of hydrocarbon generation through control of mineral surface contact area on clay catalysis. Geochem. Cosmochim. Acta 220, 429–448. https://doi.org/10.1016/j.gca.2017.10.012.

Rahman, M.J., Fawad, M., Mondol, N.H., 2020. Organic-rich shale caprock properties of potential CO2 storage sites in the northern North Sea, offshore Norway. Mar. Pet. Geol. 122, 104665 https://doi.org/10.1016/j.marpetgeo.2020.104665.

Rahman, M.J., Lebedev, M., Mondol, N.H., 2021. Nanoscale mechanical properties of organic-rich Draupne shale caprock, offshore Norway. In: 2021 SEG Annual Meeting. SEG. https://doi.org/10.1190/segam2021-3581994.1.

Ransom, B., Kim, D., Kastner, M., Wainwright, S., 1998. Organic matter preservation on continental slopes: importance of mineralogy and surface area. Geochim. Cosmochim. Acta 62, 1329–1345. https://doi.org/10.1016/S–16-7037(98)00050–7.

Rose, C., Smith, M.D., 2002. Mathematical Statistics with Mathematica. Springer Texts in Statistcs.

Sabtan, A.A., 2005. Geotechnical properties of expansive clay shale in Tabuk, Saudi Arabia. J. Asian Earth Sci. 25, 747–757. https://doi.org/10.1016/j.jseaes.2004.07.003.

Schmoker, J.W., Hester, T.C., 1983. Organic carbon in Bakken Formation, United States portion of Williston Basin. AAPG Bull. 67, 2165–2174.

Shitrit, O., Hatzor, Y.H., Feinstein, S., Palchik, V., Vinegar, H.J., 2016. Effect of kerogen on rock physics of immature organic-rich chalks. Mar. Pet. Geol. 73, 392–404. https://doi.org/10.1016/j.marpetgeo.2016.03.023.

Skurtveit, E., Grande, L., Ogebule, O.Y., Gabrielsen, R.H., Faleide, J.I., Mondol, N.H., Maurer, R., Horsrud, P., 2015. Mechanical testing and sealing capacity of the Upper Draupne Formation, North Sea. In: 49th US Rock Mechanics/Geomechanics Symposium, ARMA-2015-331. American Rock Mechanics Association. In: https://onepetro.org/ARMAUSRMS/proceedings-abstract/ARMA15/All-ARMA15/ARMA-2015-331/65734.

Skurtveit, E., Miri, R., Hellevang, H., 2018. Geological Carbon Storage: Subsurface Seals and Caprock Integrity. American Geophysical Union. https://doi.org/10.1002/9781119118657.

Teixeira, M.G., Donzé, F., Renard, F., Panahi, H., Papachristos, E., Scholtes, L., 2017. Microfracturing during primary migration in shales. Tectonophysics 694, 268–279. https://doi.org/10.1016/j.tecto.2016.11.010.

Vandenbroucke, M., Largeau, C., 2007. Kerogen origin, evolution, and structure. Org. Geochem. 38, 719–833. https://doi.org/10.1016/j.orggeochem.2007.01.001.

Vega, B., Kovscek, A.R., 2019. A systematic study of internal gas generation in shale source rocks using analogy experiments. J. Pet. Sci. Eng. 173, 209–221. https://doi.org/10.1016/j.petrol.2018.10.006.

Vernik, L., 1994. Hydrocarbon-generation-induced microcracking of source rocks. Geophysics 59, 555–563. https://doi.org/10.1190/1.1443616.

Voltolini, M., Franklin, J.G.A., 2020. The sealing mechanisms of a fracture in Opalinus clay as revealed by in situ synchrotron X-Ray Micro-tomography. Front. Earth Sci. 8, 1–13. https://doi.org/10.3389/feart/2020.00207.

Whipp, P.S., Jackson, C.A.-L., Gawthorpe, R.L., Dreyer, T., Quinn, D., 2014. Normal fault array evolution above a reactivated rift fabric; a subsurface example from the northern Horda Platform, Norwegian North Sea. Basin Res. 26, 523–549. https://doi.org/10.1111/bre.12050.

Zadeh, M.K., Mondol, N.H., Jahren, J., 2017. Velocity anisotropy of Upper Jurassic organic-rich shales, Norwegian Continental Shelf. Geophysics 82, 61–75. https://doi.org/10.1190/GEO2016-0035.1.

Zargari, S., Wilkinson, T.M., Packard, C.E., Prasad, M., 2016. Effect of thermal maturity on elastic properties of kerogen. Geophysics 81, M1–M6. https://doi.org/10.1190/GEO2015-0194.1.

Zeszotarski, J.C., Chromik, R.R., Vinci, R.P., Messmer, M.C., Michels, R., Larsen, J.W., 2004. Imaging and mechanical property measurements of kerogen via nanoindentation. Geochem. Cosmochm. Acta 20, 4113–4119. https://doi.org/10.1016/j.gca.2003.11.031.

Ziegler, P.A., 1992. North Sea rift system. Tectonophysics 208, 55–75. https://doi.org/10.1016/0040-1951(92)90336-5.